# Aerosol optical characteristics and their vertical distributions under enhanced haze pollution events: effect of the regional transport of different aerosol types over eastern China

Tianze Sun[1], Huizheng Che[1], Bing Qi[2], Yaqiang Wang[1], Yunsheng Dong[3], Xiangao Xia[4,5], Hong Wang[1], Ke Gui[1], Yu Zheng[6], Hujia Zhao[1], Qianli Ma[7], Rongguang Du[2], Xiaoye Zhang[1]

[1] State Key Laboratory of Severe Weather (LASW) and Institute of Atmospheric Composition, Chinese Academy of Meteorological Sciences, CMA, Beijing 100081, China
[2] Hangzhou Meteorological Bureau, Hangzhou 310051, China
[3] Key Laboratory of Environment Optics and Technology, Anhui Institute of Optics and Fine Mechanics, Chinese Academy of Science, Hefei 230031, China
[4] Laboratory for Middle Atmosphere and Global Environment Observation (LAGEO), Institute of Atmospheric Physics, Chinese Academy of Sciences, Beijing, 100029, China
[5] School of Geoscience University of Chinese Academy of Science, Beijing, 100049, China
[6] Collaborative Innovation Center on Forecast and Evaluation of Meteorological Disasters, Nanjing University of Information Science & Technology, Nanjing 210044, China
[7] Lin' an Regional Air Background Station, Lin' an 311307, China

*Correspondence to*: Huizheng Che (chehz@camscma.cn)

**Abstract.** The climatological variation of aerosol properties and the planetary boundary layer (PBL) during 2013–2015 over the Yangtze River Delta (YRD) region were investigated by employing ground-based Microwave Pulse Lidar (MPL) and CE-318 sun-photometer observations. Combining MODIS and CALIPSO satellite products, enhanced haze pollution events affected by different types of aerosol over the YRD region were analyzed through vertical structures, spatial distributions, backward trajectories, and the Potential Source Contribution Function (PSCF) model. The results show that aerosols in the YRD are dominated by fine-mode particles, except in March. The aerosol optical depth (AOD) in June and September is higher due to high single scattering albedo (SSA) from hygroscopic growth, but is lower in July and August due to wet deposition from precipitation. The PBL height (PBLH) is greater (means ranging from 1.23 to 1.84 km) and more variable in the warmer months of March to August, due to the stronger diurnal cycle and exchange of heat. Northern fine-mode pollutants are brought to the YRD at a height of 1.5 km. The SSA increases blocking the radiation to the surface, and cooling the surface, thereby weakening turbulence, lowering the PBL, and in turn accelerating the accumulation of pollutants,

29  creating a feedback to the cooling effect. Originated from the deserts in Xinjiang and Inner Mongolia, long-range transported

30  dust masses are seen at heights of about 2 km over the YRD region with an $SSA_{440nm}$ below 0.84, which heat air and upraise

31  PBL, accelerating the diffusion of dust particles. Regional transport from biomass burning spots to the south of the YRD

32  region bring mixed aerosol particles at a height below 1.5 km, resulting in an $SSA_{440nm}$ below 0.89. During the winter, the

33  accumulation of local emission layer is facilitated by stable weather condition, staying within the PBL even below 0.5 km.

34  **1.    Introduction**

35      Aerosol particles influence Earth's radiation budget and play a significant role in global and regional climate change

36  (Hansen et al., 1997;Che et al., 2015a;Zhang et al., 1998;Li et al., 2016). Despite numerous studies on aerosols, there is still

37  much uncertainty surrounding aerosol optical properties in relation to current assessments and predictions of global climatic

38  change (Ipcc, 2007;Stocker et al., 2013). The frequent occurrence of regional pollution demands worldwide attention

39  because of the serious consequences it can have on visibility and human health (Wu et al., 2012;Sun et al., 2016;Chan and

40  Yao, 2008).

41      The planetary boundary layer (PBL) is a critical component of Earth's climate system (Medeiros et al., 2005). The PBL

42  is directly coupled with the land surface, and its height (PBLH) plays a significant role in determining the vertical

43  distributions of aerosol particles (Deardorff, 1972). The higher the accumulation of ambient aerosols, the less solar radiation

44  reaches the surface, which will further restrict the development of the PBL, thus compounding the air pollution near the

45  surface during prolonged stagnant weather conditions (Gao et al., 2015;Petäjä et al., 2016;Leng et al., 2015). Lidar measures

46  the intensity of backscattered light as a function of distance from the instrument. The change in backscatter across the top of

47  the boundary layer provides a convenient means of determining the PBLH. Long-term, continuous PBLHs are provided by

48  Micro Pulse Lidar (MPL) observations to ascertain seasonal variations (Ku et al.;Lewis et al., 2013).

49      To analyze the spatiotemporal distribution of aerosol optical properties, multiple measurements from diverse angles

50  have been conducted by researchers worldwide. Satellite remote sensing and ground-based observations are two approved

51  ways of monitoring the long-term variation of Earth's aerosol properties (Holben et al., 2001;Che et al., 2015a) used

52 ground-based Cimel sun-photometers and found a decreasing trend in aerosol optical depth (AOD) from 2006 to 2009, but

53 an increase of ~0.03 from 2009 to 2013 in China. Chauvigné et al. (2016) compared aerosol extinction with continuous

54 high-altitude near-surface *in situ* measurements and low-altitude ground-based remote sensing atmospheric column

55 measurements over a one-year period at the Puy de Dôme station, utilizing several *in situ* instruments such as the Cimel

56 sun-photometer for the whole column, and lidar for vertical multi-altitude. Wu et al. (2017) used a variety of ground-based

57 instruments and satellite sensors, including Moderate Resolution Imaging Spectroradiometer (MODIS), Atmospheric

58 Infrared Sounder (AIRS), Cloud-Aerosol Lidar and Infrared Pathfinder Satellite Observation (CALIPSO), and Ozone

59 Monitoring Instrument (OMI) products, to detail an integrated observation of an agricultural biomass burning episode in

60 Nanjing, China. Along with the observations, trajectory models (e.g. HYSPLIT) for air mass tracking and potential source

61 apportionment have been applied to analyze the origins of aerosols (Wang et al., 2006b).

62   The Yangtze River Delta (YRD) region is a key economic and cultural hub in China, with progressive development

63 resulting in further particle emissions from industry and other anthropogenic activities. Many studies have been conducted

64 on the aerosol optical properties and their variations in the cities of the YRD, such as Shanghai, Nanjing, Lin'an, and Taihu

65 (Xia et al., 2007;Pan et al., 2010;He et al., 2012;Ding et al., 2013;Liu et al., 2015). Particularly in Hangzhou, the capital city

66 of Zhejiang province, some researches have focused on determining the seasonal variation of aerosol properties, chemical

67 compositions, and PM concentrations (Qi, 2016;Ming et al., 2017;Xiao et al., 2011), or single-case analyses on features of

68 one pollution process (Chen et al., 2012;Fu et al., 2014;Li et al., 2015). However, research into the sources of pollutants in

69 the YRD region is still needed to understand the mechanisms underlying haze pollution. Among these studies, there is a lack

70 of long-term analysis of aerosols and their sources. In addition, single-case analysis is insufficiently representative for a site

71 that experiences frequent haze occurrence. There is a lack of comprehensive studies in process analyzing from multiple

72 aspects. In particular, studies in the YRD urban area have been based almost exclusively on data from *in situ* measurements,

73 or on whole-column measurements that do not resolve the vertical distribution. This can be obtained from satellite

74 monitoring or ground-based lidar measurements. The retrieved time–height cross section of the extinction coefficient can

75 reflect the vertical distribution and structure of the aerosol layer continuously, which will contribute to optimizing the

76 satellite retrieval algorithm, and to verifying and improving the results from both satellites and models.

77    In this study, multiple data sources are analyzed to further understand the mechanisms underlying haze pollution

78    affected by different aerosol transportation over the YRD region in eastern China. Hangzhou is selected as a representative

79    site. The remainder of the paper is organized as follows: in section 2, the methods and data are presented; in section 3,

80    seasonal aerosol optical properties, PM concentrations, and PBLHs from 2013 to 2015 are analyzed to illustrate the general

81    aerosol characteristics over the urban area of the YRD; in section 4, four typical haze pollution episodes affected by different

82    types of aerosol transported to the urban area of the YRD are analyzed with ground-based sun-photometer and MPL data for

83    the obtaining optical properties and vertical distribution, satellite data from MODIS and CALIPSO for confirming the

84    observed results, PM concentration data to build an overview of the spatial distribution of pollutants in eastern China, and

85    reanalysis data for depicting the wind fields and calculating backward trajectories and potential source contributions; and in

86    section 5, a brief summary is given.

## 2.    Methods and data

### 2.1 Ground-based sun-photometer and lidar measurements

89    In this study, the aerosol optical properties were measured in Hangzhou (30°14'N, 120°10'E, 41.7 m above sea level).

90    This site lies in the West Lake scenic area, which is a commercial and residential area in the southern part of the city (Fig. 1).

91    The AOD at 440, 670, 870, and 1020 nm was measured from January 2013 to December 2015 using a CE-318

92    sun-photometer with a 1.2° full field-of-view (Holben et al., 1998). The validated AOD data presented in this article were

93    obtained using the ASTPwin software developed by Cimel Co. Ltd. (Che et al., 2013) for level 1.5 AOD (cloud-screened).

94    Aerosol optical properties were processed using the method of Dubovik et al. (2000) and Dubovik and King (2000), based

95    on the almucantar measurement data of the Cimel sun-photometer. The Cimel sky radiance measurements taken at 440, 670,

96    870, and 1020 nm, in conjunction with direct sun AOD data collected at these same wavelengths, were used to retrieve

97    volume aerosol size distributions (dV/dln(r) in the size range 0.05 to 15 μm), single scattering albedo (SSA) values,

98    Ångström exponent (AE), absorption AOD (AAOD), and volume concentrations of fine- and coarse-mode aerosols (Eck et

99    al., 2010;Che et al., 2014). Only SSA and AAOD results with $AOD_{440nm} > 0.40$ were used due to the high uncertainties

100    inherent in lower AOD values (Che et al., 2015b).

101    The ground-based lidar instrument used was the MPL installed at the Hangzhou National Reference Climatology

102    Station. The MPL produced by Sigma Space Corporation is an elastic back-scattering lidar, equipped with a 532-nm

103    wavelength laser launcher. In this study, aerosol measurements were obtained with a 30-m range resolution and a 30-s

104    accumulation time, and a blind area of detection existed ranging from 200 to 300 m. The aerosol extinction coefficient

105    profiles, PBLH, and AOD were retrieved during 2013–2015 using the algorithm of (Fernald, 1984), which considers the

106    atmosphere to be comprised of aerosols and air molecules (Liu et al., 2016).

107    **2.2 MODIS and CALIPSO data**

108    The MODIS instrument operates on both the Terra and Aqua satellites. In this study, to illustrate the spatial distribution

109    of AOD, we used the daily AOD combined dark target and deep blue data at 550 nm for land and ocean from MODIS Level

110    3 Atmosphere Products, during 9–15 October 2015 (Levy et al., 2007a;Levy et al., 2007b). Global MODIS hot spots detected

111    during 6–13 August 2013 in China were obtained from the Fire Information for Resource Management System for fire

112    locations (https://firms.modaps.eosdis.nasa.gov/).

113    The products of CALIPSO were used for this study, and these are available from the NASA Langley Research Center

114    (https://www-calipso.larc.nasa.gov/). The primary instrument carried on the CALIPSO satellite is the Cloud-Aerosol Lidar

115    with Orthogonal Polarization (CALIOP). In this work, we selected the V4.10 CALIOP Level 2 data products to acquire the

116    images of vertical feature masks and aerosol subtypes    (Omar et al., 2009;Winker et al., 2009;Vaughan et al., 2004).

117    **2.3 Reanalysis data for the PBLH and wind field**

118    The reanalysis data for the PBLH and wind fields were downloaded from the European Centre for Medium-Range

119    Weather Forecasts (ECMWF), ERA-Interim (http://apps.ecmwf.int/datasets/). The monthly-average PBLH values were from

120    2013 to 2015, and the daily wind fields were analyzed at different pressure levels with a spatial resolution of 0.5 ° × 0.5 °.

**2.4 Surface *in situ* PM$_{2.5}$ and PM$_{10}$ data**

In 2012, the China National Environmental Monitoring Center began to make hourly observations of PM$_{2.5}$, PM$_{10}$, and other atmospheric pollutants in 367 major cities in China (http://106.37.208.233:20035/). In this work, the hourly data were processed to obtain the daily and monthly PM$_{2.5}$ and PM$_{10}$ concentration results during 2013–2015.

**2.5 Backward trajectory, PSCF and CWT analysis**

Three-dimensional 72-h air mass backward trajectories at multiple altitudes over Hangzhou every 6 h (0000, 0600, 1200, and 1800 UTC) were calculated using the NCEP FNL (National Centers for Environmental Prediction Final Analyses) archive data. The software used was TrajStat (http://www.meteothinker.com/products/trajstat.html) (Ngan et al., 2015). The cluster methods of air mass backward trajectories from Sirois and Bottenheim (1995) were applied to confirm the major transport pathways.

To determine the pollutants' source locations and prevailing transport pathways, backward trajectories combined with PM concentrations [referred to as the Potential Source Contribution Function (PSCF) model and Concentration Weighted Trajectory (CWT) model] were used. A weighting function was applied to better reflect the uncertainty in the values, and this is referred to as WPSCF and WCWT in each model, respectively (Polissar et al., 1999;Hsu et al., 2003;Xin, 2016;Seibert et al., 1994). The specifics of the two models' parameters and algorithms have been described in detail by Wang et al. (2006b).

**3. Results and discussion**

**3.1. Variation in PM$_{2.5}$ and PM$_{10}$ mass concentration**

Figure 2a shows the monthly variation in mass concentrations of PM$_{2.5}$ and PM$_{10}$ and the proportion of PM$_{2.5}$ to PM$_{10}$ during 2013–2015 in Hangzhou. It can be seen that mass concentrations of PM$_{10}$ and PM$_{2.5}$ in the YRD region are distinctly higher in January (129.39 μg/m$^3$), November (96.32 μg/m$^3$), and December (119.16 μg/m$^3$) than in other months, while the PM$_{2.5}$:PM$_{10}$ ratio during these months plus February also exceeds other months, ranging from 76.1% to 86.6%. Meanwhile,

142  the lowest concentrations occur in July and August, which can result from wet deposition due to the abundant precipitation at

143  this time of year (Jacob and Winner, 2009). These results verify the findings of Ming et al. (2017), Cao et al. (2009), and

144  Wang et al. (2006a), that the highest and lowest $PM_{2.5}$ mass concentrations occur respectively during the winter and summer

145  in the YRD region. For the other months, concentrations of $PM_{10}$ are high but the $PM_{2.5}$ accounts for less than 65% during

146  March to May.

147  **3.2 Variation in aerosol optical properties**

148      Figure 2b depicts the monthly means of the AE between 440 nm and 870 nm, and the AOD at four different

149  wavelengths (440, 670, 870, and 1020 nm) in Hangzhou during 2013–2015, retrieved from the CE-318 sun-photometer. The

150  monthly variation trends of AOD means at the four wavelengths are consistent, and the values of $AOD_{440nm}$ are the highest

151  among them. The averaged $AOD_{440nm}$ values during January to May are about 0.8, and the AOD values at the four

152  wavelengths reach their maxima in June at 1.20 $\pm$ 0.55, 0.76 $\pm$ 0.37, 0.54 $\pm$ 0.25, and 0.43 $\pm$ 0.20, respectively. After June,

153  AODs reduce to less than 0.8, and in August the mean values reach their minima at 0.59 $\pm$ 0.34, 0.32 $\pm$ 0.21, 0.23 $\pm$ 0.14, and

154  0.18 $\pm$ 0.10, respectively. In September, the values increase again to 1.07 $\pm$ 0.54, 0.63 $\pm$ 0.38, 0.43 $\pm$ 0.26,     and   0.32   $\pm$

155  0.20, respectively, after which the $AOD_{440nm}$ means decrease below 0.8 during October to December.

156      In general, AODs in June and September are relatively high, yet in July and August they are lower than in other months.

157  The results of July and August agree with Qi (2016) that the lowest AOD appears in summer, with a mean value of 0.72 $\pm$

158  0.58 at 440 nm in Hangzhou. According to Che et al. (2014), the relatively low PM mass concentrations may result from the

159  substantially increased precipitation in the YRD region in summer (including July and August) due to the summer monsoon,

160  which can decrease the concentration of atmospheric aerosols through wet deposition. This pattern has also been observed in

161  Taihu and Lin'an (Pan et al., 2010). Because the subtropical anticyclone begins to move north and precipitation decreases

162  from the end of August to the beginning of September, the AOD increases in September. Nevertheless, the peak in the

163  monthly AOD means in Pudong occurs in June, which may derive from the stable weather caused by the lack of strong

164  winds (Duan and Mao, 2007).

165    The monthly mean AEs ($AE_{440nm–870nm}$) vary almost inversely to the AOD, and are all greater than 0.8, which indicates

166    that the AODs are dominated by fine particles in the YRD region during 2013–2015 (Qi, 2016;Eck et al., 2012). When

167    $AE_{440nm–870nm}$ is greater than 0.8 at East Asian sites, fine-mode aerosols emitted from population centers in East Asia

168    dominate the aerosol optical properties even on spring dust days, during which pollution aerosols are mixed with

169    coarse-mode particles. Comparing the bars' heights in the figure, the minimum monthly averaged $AE_{440nm–870nm}$ occurs in

170    March (1.16 ±0.24), and the maximum in September (1.41 ±0.25). This shows the influence of long-distance dust transport

171    from the desert districts located in northern and northwestern China (Zhang and Li, 2012;Gong et al., 2003), which can have

172    an influence on the YRD region.

173    Figure 2c shows the monthly volume size distributions of aerosols during 2013–2015 in Hangzhou. In general, the size

174    distributions show a bimodal logarithm normal structure: a fine mode with radius < 0.6 μm and coarse mode with radius >

175    0.6 μm (Dubovik et al., 2002). Nevertheless, in June and September, the distribution appears tri-modal,  indicating a

176    tendency for hygroscopic growth in fine-mode particles in the YRD region (Pilat and Charlson, 1966). In June and

177    September, the fine modes reach maximum peaks at a radius of 0.34 μm, while other months' peaks occur at a radius of 0.15

178    μm. As for the coarse mode, March, April, November, and December peaks occur at a radius of 2.24 μm, while the peak

179    radius during the other months is larger than 2.24 μm. Because of the dust transport, coarse modes dominate in March, while

180    in July, August, and September the coarse mode only contributes a small fraction. Conversely, the fine particles play a

181    leading role in the other months, particularly in June and September. This situation may arise due to the mixed influence of

182    hygroscopic growth, coagulation growth, and different species of aerosols emitted from various sources (Li et al., 2007;Zhu

183    et al., 2014;Che et al., 2014). Hygroscopic properties of ambient particles in urban Hangzhou are mainly a function of their

184    size and chemical composition (Zhang et al., 2011). Since the highest AOD values are seen in June (but not in July and

185    August), it is suggested that the hygroscopic growth in the fine mode leads to enhanced scattering, which significantly raises

186    the AOD values in the YRD region.

187    The SSA is defined as the ratio of the scattering coefficient to the extinction coefficient, and is one of the key

188    parameters used in assessing the radiation effect on climate change (Jacobson, 2000). Highly absorbing particles, including

189    urban-industrial aerosols, have a warming effect, while low absorbing particles such as dust can have a cooling effect

190 (Dubovik et al., 2002). Figure 2d shows the monthly variation of SSA at the 440-, 670-, 870-, and 1020-nm wavelengths.

191 From September to February, the SSAs at the four wavelengths are close and relatively high. However, over the warmer

192 months of March to August, the values decrease and the difference between the wavelengths becomes greater, particularly in

193 July and August with low SSA, which may imply that the low-SSA particles are more sensitive to the wavelength variability.

194 The minimum SSAs occur in August at $0.869 \pm 0.095$, $0.839 \pm 0.114$, $0.793 \pm 0.149$, and $0.762 \pm 0.169$, respectively; the

195 maximum is in September, with the highest value of $0.963 \pm 0.033$ at 440 nm. As a result, the aerosols in the YRD region

196 during August tend to be absorbing, but during September the hygroscopic aerosol particles become more capable of light

197 scattering through condensation and evaporation of water vapor (Adachi et al., 2015), which may result from the variability

198 of the aerosols' composition and sources in the ambient atmosphere. According to the studies by Qi (2016) and Xia et al.

199 (2007), the absence of a heating period in southern China in winter causes higher SSA than in northern cities such as Beijing,

200 where biomass burning can emit black and organic carbon. According to the results of monthly AOD and the volume size

201 distribution presented in this article, the high level of AOD in September may be due to the strong scattering ability provided

202 by the prominent hygroscopic growth.

203 **3.3 Variation in the PBLH measured by lidar**

204 In this study, by utilizing the backscatter signal at 532 nm with an MPL, the PBLHs from 2013 to 2015 at Hangzhou

205 were retrieved at a 10-min temporal and 30-m spatial resolution. To verify the reliability of these PBLHs, we used the

206 monthly averaged reanalysis data of the PBL from ERA-Interim to obtain a linear fit with the PBLHs from MPL (after

207 computing the monthly average). The Pearson's correlation coefficient between these two monthly averaged series is 0.88,

208 which passes the significance test at the $p = 0.1$ level. Despite the strong correlation between the reanalysis- and the

209 MPL-derived PBLH, the values obtained from the reanalysis data are significantly lower than those from the MPL. It is

210 suggested that improvements are needed in the reanalysis data.

211 Since the PBLHs retrieved from the MPL are reliable, we adopt them to examine the monthly variation characteristics

212 in the YRD region during 2013–2015. Figure 3 shows the monthly averaged height of the PBL and its 5th and 95th

213 percentile box plots during 2013–2015 in Hangzhou. Due to the blind detection area of the MPL, the minimum value is

214 about 300 m above the surface. During the warmer months (including March to August), the monthly means of the PBLH are

215 above 1 km, and the range between the 5th and 95th percentiles is greater than 1 km, varying from above 0.5 km to about 2

216 km. Conversely, mean PBLHs in the colder months are almost below 1 km and the range between the 5th and 95th

217 percentiles is half that in the warmer months, ranging from about 0.5 km to below 1.5 km. The wider range in the warmer

218 months may result from a stronger diurnal cycle (Liu and Liang, 2010) and daily exchange of heat and mass in the PBL

219 (Medeiros et al., 2005). These characteristics help to explain the higher *in situ* PM mass concentrations in the winter months

220 than in summer discussed above.

221 **3.4 Case analysis of pollution sources**

222 For a further explanation of the monthly variation in aerosol optical properties, and to examine the variety of pollutant

223 sources affecting the enhanced haze pollution events in the YRD region, four cases with different transportation categories

224 are discussed here, combining ground-based observation, remote sensing, reanalysis, and satellite data, to build a

225 comprehensive analysis (Fig. S6 in the supplementary material).

226 **3.4.1 Pollutants transported from polluted areas in northern China**

227 A few episodes of pollutants transported from northern China were detected by the MPL, as illustrated in Fig. 4a, which

228 shows the time–height cross section of extinction coefficients in Hangzhou. The aerosol vertical distributions were further

229 assessed by extracting profiles of aerosol extinction coefficient from the MPL on a daily basis during this period (Fig. 5). On

230 the first day, 9 October 2015, the thin external aerosol layer is seen around 1 km during nighttime, when the maximum

231 extinction coefficient is more than 0.6 km$^{-1}$, and this is separate from the lower local pollutants layer. During the following

232 three days, the external aerosol masses are around 1 km at nighttime and above 1.5 km during the daytime, and appear to be

233 multilayer in structure. Meanwhile, the daily averaged PBLH is around 1.2 km and 1.5 km on 11 October and 12 October

234 respectively, sitting above the aerosol layer at nighttime and beneath it during the day (Fig. 6). With the PBL pushing down,

235 the aerosol layer begins to descend from the afternoon of 12 October, continues to descend to below 1 km until 15 October,

236 and then mixes downwards into the local emissions aerosol layer. Concurrently, the peak extinction coefficients vary from

237 0.2 to 0.5 km$^{-1}$, reaching their maxima when the external and local pollutants mix together in the PBL. To verify the

238 significance of the PBL in this process, the Pearson's correlation coefficient between the daily averaged PBLH from the

239 MPL and the daily mass concentration of PM$_{2.5}$ during 9–15 October was computed. The result appears negative, at −0.88

240 (passing the significance test at the $p = 0.1$ level), which indicates that the descending PBL accelerates the accumulation of

241 PM mass from the two aerosol layers in it.

242 Aerosol optical properties from the CE-318 retrieval data are exhibited in Fig. 6. According to the pattern of volume

243 size distribution during 11–15 October 2015, the fine mode dominates, which can be referred to the volume of both modes as

244 well, and the peak radius growth from 0.11 to 0.15 μm is attributable to the hygroscopic growth, which may help strengthen

245 the scattering ability of the particles (SSA is up to 0.96 at 440 nm). The daily averaged AODs at 440 nm are all above 0.65

246 during this process. On 15 October, the AOD is close to 1.00 at 440 nm when the two aerosol layers mix. The SSAs at all

247 four wavelengths continue to increase from 11 to 14 October, and decrease on 15 October. The values at 440 nm vary from

248 0.95 to around 0.97. The AAODs show a corresponding variability trend with AOD and the volume of the coarse mode,

249 which dominates the absorbing features. The maximum AAOD at 440 nm is 0.056 on 12 October, and the minimum is 0.026

250 on 14 October.

251 Due to the continuous aerosol-transport signals detected by the MPL during 9–15 October 2015, trajectories over this

252 period were grouped into three clusters, as depicted in Fig. 7a-1. Cluster-1 contributes the maximum proportion of 50.00%

253 and comes from northern China, via Hebei, western Shangdong and Jiangsu province, travelling southwards to the YRD

254 region. This cluster relates to the highest PM$_{2.5}$ concentration (81.05 ± 28.18 μg/m$^3$). Cluster-2 travels on the lowest and

255 fastest stems from north of Anhui province, accounts for 30.95%, and correlates with the PM$_{2.5}$ concentration of 74.45 ±

256 30.17 μg/m$^3$. The highest air mass trajectories associated with cluster-3 account for 19.05% and originate from the eastern

257 edge of Xinjiang at an altitude above 5000 m, also passing through Henan and Anhui province to Hangzhou.

258 The WPSCF reveals the spatial distribution of the probabilities of the potential PM$_{2.5}$ sources obtained by the HYSPLIT

259 model and PM$_{2.5}$ concentrations. As shown in Fig. 7a-2, the most likely source areas with WPSCF values for PM$_{2.5}$ cover

260 most of Henan, Anhui, Jiangsu, and Shangdong provinces, in which the WPSCF values are over 0.8. Figure 7a-3 shows the

261 spatial distribution of the WCWT value, which provides information regarding the relative contribution of source regions

262 potentially affecting $PM_{2.5}$ (> 35 μg/m$^3$) in Hangzhou, similar to the WPSCF pattern. The northern part of Henan and the

263 western Shangdong region (including the south of the Beijing–Tianjin districts), with rather high WCWT values (> 75 μg

264 m$^{-3}$), is recognized as the area contributing the most $PM_{2.5}$. Combining the daily spatial distribution of $PM_{2.5}$ concentrations

265 with AOD from MODIS retrieval data over eastern China (Figs. S1–S2 in the supplement), districts where the air mass

266 trajectories pass intensively can be seen to have relatively high pollution levels. These include Henan, Hebei, Anhui, and

267 Jiangsu provinces, situated in the North China Plain, which has been recognized as another center of high $PM_{2.5}$

268 concentrations (Zhang et al., 2012;Zhang et al., 2013). Besides, the pollution scope from north to the YRD region is wider

269 and more serious day by day.

270 Furthermore, daily wind fields at 850 hPa (height of about 1.5 km, at which the transport is detected by the MPL) from

271 ECMWF (Fig. S1 in the supplementary material) verify the northwest wind prevailing over eastern China during this case,

272 which brought the pollutants from northern China to the YRD region. The wind speed gradually declines, benefiting the

273 formation of stable conditions during the last few days. Note that CALIPSO's acquisition of the aerosol vertical distribution

274 on 14 October is consistent with the above results that an aerosol layer under 2 km exists over Hangzhou and the areas

275 further north (where intensive trajectories passed over), and is identified as "polluted continental" or "polluted dust" (Fig.

276 8a). Under certain circumstances, however, smoke aerosols can be misidentified as "polluted dust" aerosols (Xia et al.,

277 2013).

278 Although a dry, clean northwestern airstream prevails in eastern China during winter (Tao et al., 2012), northern winds

279 near the surface may not be strong enough to blow the pollutants away from eastern China, but transport the particle

280 pollutants to the central part of the North China Plain. The continuing northwesterly winds blow particle pollutants to the

281 YRD region (Li et al., 2014;Ming et al., 2017). A similar transport mechanism occurs in this case during 9–15 October 2015.

282 Northerly pollutant transport at 850 hPa primarily results in an increase in $PM_{2.5}$ mass concentration, which is facilitated by

283 the occurrence of the descending external aerosol layers, pushed down by the PBL. Pollutants from the North China Plain

284 are dominated by fine particles, which tend towards hygroscopic growth with adequate requisite moisture in the YRD region,

285 increasing the SSA over Hangzhou. As a result, the increasing scattering aerosols transported from haze areas of North China

block the solar radiation to the surface, creating a cooling effect. If that is the case, turbulence will correspondingly weaken, and the PBLH will decrease, facilitating the accumulation of pollutants at lower heights. The accumulation of air pollutants can then intensify the scattering ability, forming a positive feedback mechanism.

**3.4.2 Pollutants transported from desert areas**

Dust events in spring contribute to high AODs, particularly in northern and eastern China (Che et al., 2015b). They are transported over long distances and their influence can be identified on regional and even global scales (Chin et al., 2006;Uno et al., 2009). For instance, Asian dusts are frequently observed in spring and result in air pollution in the downwind areas of East Asia (Kim et al., 2010;Sakai et al., 2002;Sakai et al., 2003;Liu et al., 2011;Li, 2015), such as the YRD region including Nanjing and Shanghai (Yong et al., 2015;Huang et al., 2013).

A series of transported aerosol masses from the northwestern desert area over the YRD region were monitored by the MPL and are seen in the time–height cross section of extinction coefficients at 532 nm during 5–9 March 2013 in Fig. 4b. Throughout this period, the volume size distributions and particle volumes are strongly dominated by the coarse mode (Fig. 10). The peak radius of the fine mode is around 0.11 μm, and 1.3 μm for the coarse mode. The AOD on 7 March is around 0.88, when the transported aerosol layer is most intense, while the value on 6 March is just 0.47 at 440 nm. Early on 5 March, the intensive layer is detected at 1.5 km and the peak extinction coefficient is around 0.65 $km^{-1}$, according to the profiles shown in Fig. 9. The SSAs retrieved from the CE-318 are 0.84, 0.91, 0.91 and 0.90 at 440, 670, 870 and 1020 nm, respectively, which are lower than those for the northern transported particles. The corresponding AAODs are 0.13, 0.05, 0.04 and 0.04, respectively, which are higher than the values during the northern transportation case. The particles in this case are more strongly absorbing than the type transported from the northern polluted areas discussed in the previous section. The transported mass weakens on the second day until night, when the aerosol layer lies between 1.0 and 2.5 km, with the peak coefficient above 0.4 $km^{-1}$. Correspondingly, the volumes of both modes decrease, and this is accompanied by a drop in SSA and AAOD to 0.79 and 0.1, respectively, at the 440 nm wavelength. During 7–8 March, a thickening of the external aerosol layer is accompanied by a substantial increase in the volume of coarse-mode particles, coinciding with an increased AAOD to 0.15 on 7 March and 0.13 on 8 March, at 440 nm. The peak extinction is about 0.2 $km^{-1}$ above a height of 2 km.

310    On the last day of this case, no external aerosol layer is detected by the MPL (the noisy signals shown in the profiles in Fig. 9

311    may result from an instrumental malfunction), and the absorption weakens due to the reduced volume. Note that the SSAs

312    show little change during the last three days, which implies that SSA may not be sensitive to the variation of particles in the

313    dominant coarse mode. Meanwhile, the PBLH above the aerosol layer varies from 2.0 km to about 3 km continuously in this

314    case, dissipating the transported dust particles and causing the peak extinction coefficients to decrease each day.

315        From the CALIPSO L2 retrieval results of vertical feature mask and aerosol subtypes (illustrated in Fig. 8b), a 3-km

316    thick aerosol layer can be seen on 5 March 2015 in the northwestern upwind areas of the YRD, with a mixture of "dust" and

317    "polluted dust". After this, a thin external layer is detected.

318        Assuming that the extraneous aerosol layer was dust, based on the *in situ* and satellite observations, 72-h backward

319    trajectory analysis was applied to determine the source of the dust. Since the dust aerosol layer is most intense at 2 km, the

320    start location of the trajectory calculation was set to be 2000 m. Figure 7b-1 shows three cluster trajectories changing with

321    height. The air masses associated with cluster-1, accounting for 55%, originate from the Gurbantunggut Desert lying in

322    northern Xinjiang, and move southeasterly over the Gobi Desert and the Badain Duran Desert located in Inner Mongolia.

323    This trajectory is similar to the dust pathway to Xi'an described by (Wang et al., 2006b). The air masses associated with

324    cluster-2, accounting for 35%, follow parallel paths from the Kumtag Desert in western Xinjiang, and pass over the Loess

325    Plateau. The cluster-3 stems from Guangxin province at an altitude below 3000 m, and does not pass over a desert area.

326        The number of trajectories in each cluster and the corresponding $PM_{10}$ mean concentrations for all trajectories are

327    summarized in Table 1. Based on the mean $PM_{10}$ concentrations in each cluster, clusters-1 and 2 take the most primary role

328    in bringing dust to the YRD region. Combining the distribution of WPSCF and WCWT values, the sources most likely to

329    affect the YRD are located in the deserts of northwestern China, termed the "Western High Dust Desert" (Zhang et al. (1998),

330    which include the Gurbantunggut Desert, the Gobi Desert, and the Badain Duran Desert, covered by cluster-1. From the

331    intensive trajectories' pathways, Henan and Anhui provinces also appear to be highly likely source regions located upwind of

332    the YRD, which just corresponds to the vertical feature mask from the CALIPSO L2 products that show a mixed layer of

333    "dust" and "polluted dust" in Anhui province. The WCWT results make the potential sources explicit. The Gobi Desert, and

334    Henan and Anhui provinces are prominent sources of dust transported to Hangzhou.

335   The daily spatial distributions of $PM_{10}$ concentrations and wind fields at 750 hPa in eastern China during 5–9 March

336   2013 are shown in Fig. S3 in the supplementary material. The *in situ* mean $PM_{10}$ concentration on 5 March is between 200

337   and 250 μg/m³, while for the remaining days it is between 150 and 200 μg/m³ in Hangzhou. The wind fields at 750 hPa show

338   northerly and northwesterly winds during 5–8 March 2013, consistent with the primary trajectories to Hangzhou at a height

339   of 2 km. The second day, 6 March, shows the lowest wind speed, coinciding with minimal horizontal transport during that

340   day, as can be seen in the time–height cross section of the MPL extinction coefficient (Fig. 4b). The wind speed over the next

341   two days increases, as does the transport. On the last day, the wind direction turns southwesterly at 750 hPa, which may

342   bring the clean air from the sea to Hangzhou. The wind direction on 9 March is consistent with the existence of cluster-3,

343   which carries little $PM_{10}$ mass and only accounts for 10% among the trajectories.

344   In spring, the long-range transport of dust aerosols from desert regions not only has an impact on northwestern cities

345   such as Xi'an (Wang et al., 2006b), or cities in the north of eastern China such as Beijing, Xianghe, and Shenyang (Jinyuan

346   et al., 2010;Zhang et al., 1998), but also on cities in the YRD region such as Nanjing, Shanghai (Zhang et al., 2016), and

347   Hangzhou. When transported dust particles dominate in the ambient atmosphere over the YRD region, the aerosol optical

348   properties show a relatively high level of absorptive features, much stronger than in aerosols transported from the north.

349   These particles mostly come from moving air masses loaded with dust particles from desert regions located in northwestern

350   China. During the days dust transport enhanced, absorptive dust particles increase AOD and AAOD over Hangzhou, and heat

351   the atmosphere to facilitate the turbulence leading the PBL lifting in the same day, which will accelerate the diffusion in the

352   following days.

353   **3.4.3 Pollutants transported from biomass burning areas**

354   Since the lowest values of SSA occur in August, the aerosol particles over Hangzhou exhibit strong absorption

355   characteristics in that month. Figure 4c illustrates the time–height cross section of extinction coefficient retrieved from the

356   MPL during the transportation of biomass-burning emissions to Hangzhou, and shows little contribution from local

357   emissions. In the first four days, the external aerosols are concentrated at 1.5 to 2 km and the peak extinctions are less than

358   0.2 km⁻¹, even during the daytime (Fig. 11). In the meantime, the PBLH varies from 2.45 km to 2.93 km, above the

359    transported aerosol layer. Over 10–11 August, the external fine particles are noticeably enhanced, with the PBLH decreasing

360    to 2.30 km. Consequently, the layer develops downwards, to a height of around 1 km, which may imply a tendency towards

361    sedimentation. Maximum extinctions exceed 0.2 km$^{-1}$, and even reach 0.3 km$^{-1}$ during the daytime on 11 August. The

362    transports tend to die down and deposit over 12–13 August, with a higher PBL, thinner aerosol layer, and lower coefficients

363    (below 0.1 km$^{-1}$). The whole process of this transportation is not as strong as the northern transport process. During 6–9

364    August, AOD values (retrieved from the CE-318) are below 0.5. They increase to 0.75 when the maximum extinction occurs

365    over 11–12 August, and decrease when diffusion and sedimentation contribute. Combined with other aerosol optical

366    properties, fine-mode particles are remarkably dominant during the whole process in terms of the volume and its size

367    distribution (Fig. 12). However, the mass concentration is far less than during the northern transported pollution of 11–15

368    October 2015. In this case, the total volumes are below 0.1 μm$^3$ for most of the days, except for the two enhanced transport

369    days in which the total volume exceeds 0.12 μm$^3$. The SSAs keep increasing until a peak value of between 0.73 and 0.898 at

370    440 nm before the last two days, which suggests that the increase in external fine particles enhances the scattering ability.

371    The values are similar to the SSAs observed from biomass-burning emissions in the African savanna, Zambia, during 1995–

372    2000 (Dubovik et al., 2002). The AAODs are almost above 0.09 at 440 nm during this period, which is higher than those

373    seen in the northern transported pollution. It is suggested that the particles brought by these air masses are fine mode, with

374    strong absorption characteristics, which is indicative of smoke aerosol.

375        To determine the pollution source, trajectories and primary clusters are depicted in Fig. 7c-1, with the

376    backward-trajectory start locations set to 1000 m, 1500 m, and 2000 m. Considering the significant absorptive ability of

377    aerosol particles transported over Hangzhou, we apply the fire hotspot information (90% confidence) from MODIS

378    Collection 6 and VIIRS 375 m to analyze the possible source of this type of particle. It is assumed that the external particles

379    during these days were created from biomass burning, which is the major source of atmospheric light-absorbing organic

380    carbon and black carbon aerosols, contributing around 42% of the global black carbon emissions (Bond et al., 2004;Bond et

381    al., 2013;Cao et al., 2005). Combining the fire spots detected by MODIS with the trajectory analysis, the majority of

382    trajectories (accounting for 69.79%), which are associated with cluster-1, travel northeasterly to the YRD region, passing

383    over fire spots located in Guangdong, Fujian, Jiangxi, and Zhejiang provinces, with a mean PM$_{2.5}$ concentration of 54.52 ±

384  16.63 μg/m$^3$. According to the study of (Chan, 2017), not only do the biomass burning emissions have local impacts, but they

385  can also be transported intercontinentally and influence the atmospheric system on a global scale. The air masses associated

386  with cluster-2 originate from the sea to the southeast, only passing one spot lying in southern Zhejiang with a mean PM$_{2.5}$

387  concentration of 39.04 ±10.14 μg/m$^3$, bringing clean air from over the sea to Hangzhou during 12–13 August (Fig. S5 in the

388  supplementary material).

389      With reference to the WPSCF and WCWT results, the locations of the potential sources are almost consistent with the

390  regions where fire spots are detected or biomass burning occurs, including the eastern part of Guangdong and Jiangxi

391  provinces, western Fujian, and most of Zhejiang. The occurrence of biomass burning in these areas has been studied

392  previously (Wang and Zhang, 2008). With regard to the retrieval results of the vertical feature mask and aerosol subtype

393  from CALIPSO on 5 August (Fig. 8c), the intensive aerosol layer exists below 2 km along the CALIPSO path southwest of

394  Hangzhou. The aerosol types are mostly identified as "polluted continental" or "polluted dust" over and southwest of

395  Hangzhou, which coincides with the backward trajectories carrying pollutants from the fire spots during 6–13 August 2013.

396  As has been noted, the retrieval results from CALIPSO may misidentify the smoke aerosols as "polluted dust", but for the

397  majority of days during this case satellite retrieval data verify the results from CALIPSO.

398      The aerosol transported from the southern biomass-burning areas to Hangzhou shows a capacity for strong light

399  absorption, and is dominated by the fine mode. The external aerosol layers observed in the vertical distribution of the

400  extinction coefficient appear around 1–2 km, with the maximum value at 0.3 km$^{-1}$. The backward trajectory and potential

401  source analysis determine the likely sources. Satellite retrieval results (both MODIS and CALIPSO) verify that the

402  transported aerosol originates from biomass-burning regions, and this is consistent with the aerosol optical properties

403  retrieved from the CE-318 in Hangzhou. In addition, previous studies have shown that aerosol absorption depends on the

404  mixing mechanism of soot with other aerosol components (Ackerman and Toon, 1981;Martins et al., 1998;Jacobson, 2001),

405  so the situation that occurs during 6–13 August 2013 is not unique to the YRD region.

### 3.4.4 Pollutants emitted from local emissions

406

407    While aerosols transported from the northern, southern or desert areas contribute much to the ambient atmospheric

408    pollution in the YRD region, a high concentration of aerosols with diverse properties is also emitted locally (Chen et al.,

409    2012;Zhuang et al., 2015;Liu et al., 2015).

410    Figure 4d shows a series of successive local emissions in the time–height cross section of the extinction coefficient

411    obtained by the MPL, during 27–29 December 2013. The PBLH varies from 1.16 to 0.72 km during this period. It can be

412    seen that the aerosol is composed of two layers, distributed below and above the PBL. An external aerosol layer can be seen

413    at 1–1.5 km, while the layer caused by local emissions lies below 1 km, and even below 0.5 km, due to the stable PBL that

414    exists over cold surfaces, particularly in the winter time (Medeiros et al., 2005). From the vertical profiles of the extinction

415    coefficient in Fig. 13, 27 December 2013 sees the peak extinction of the local emissions layer, at around 0.1 and 0.15 km$^{-1}$ in

416    the nighttime and daytime, respectively. The two separated layers mix downwards on the second day, so that the profiles

417    barely show the separation between them, and the maximum extinction coefficient reaches 0.2 km$^{-1}$ below 0.5 km. On 29

418    December, an intensification is seen both in aerosols transported at higher altitudes and in those emitted locally, and the peak

419    coefficient for the local emissions layer is close to 0.4 km$^{-1}$ during the daytime and 0.2 km$^{-1}$ at night.

420    The AODs retrieved from CE-318 vary from 0.4 to 0.55, according to the results presented in Fig. 14. The volume size

421    distribution during these three days shows a strong bimodal pattern, with the peak volumes at radii of 0.11 μm and 2.94 μm

422    for fine and coarse modes, respectively. Coarse particles noticeably dominate on 27 December, with an SSA of 0.89 at 440

423    nm—lower than the value at other wavelengths. Meanwhile, satellite retrieval results of vertical feature mask and aerosol

424    subtype from CALIPSO (Fig. 8d) verify the dominance of the coarse mode on 27 December. The L2 products confirm the

425    existence of an aerosol layer below 2 km, and identify it as mixed "polluted dust" and "polluted continental" over the YRD

426    region. Furthermore, another layer identified as "dust" exists between the heights of 3 and 5 km (beyond the detection range

427    of the MPL), composed of high-volume coarse mode particles, which may have an influence on the lower "polluted dust"

428    layer. Over the next two days, the volume of the two modes become more balanced due to enhanced transport and emissions,

429    and the SSAs at 440 nm show an inverse relationship to the values at other wavelengths. On 29 December, the lowest value

430  of SSA (440 nm), at 0.88, and the highest value of AAOD (440 nm), at 0.073, is seen. The maximum SSA value in this case

431  is higher than the peak SSA observed when desert transport occurs, but lower than the peak value seen with the strong

432  biomass-burning transport. The aerosol optical properties of mixed fine- and coarse-mode particles are different from when

433  one mode dominates.

434      With reference to the spatial distribution of $PM_{2.5}$ mass concentration and the wind field at 10 m from the surface (Fig.

435  S5 in the supplementary material), the enhanced emissions seen in the extinction coincide with an increase in the *in situ*

436  observed PM concentration during 28–29 December. The wind is low within the PBL due to the weakening of atmospheric

437  circulation in northern China during winter (Tao et al., 2016). Consequently, the low wind speed at the surface contributes to

438  the accumulation of aerosol particles, resulting in an increase in pollutant concentrations over these days.

439      Pollutants emitted locally stay below 0.5 km during 27–29 December 2013 in the YRD region. Facilitated by the low

440  wind speed at the surface and the downward transport of external dust aerosols, aerosol optical properties show weaker

441  absorption than the strong biomass-burning aerosol, and weaker scattering than transported dust aerosols.

442  **4.  Conclusion**

443      Based on long-term ground-based lidar and sunphotometer observations, variations in monthly averaged aerosol

444  properties and PBLHs during 2013–2015 in the YRD region are presented and discussed. Combining satellite remote sensing

445  data from CALIPSO and MODIS, backward trajectories, and PSCF and CWT analyses, four typical transportation

446  mechanisms are analyzed under enhanced haze pollution events in the YRD region.

447      For the long-term monthly variation of aerosol optical properties in the YRD region, it is found that fine and scattering

448  particles dominate, except in March. The $PM_{2.5}$:$PM_{10}$ ratio is high, $AE_{440nm–870nm}$ is above 0.8, and SSA exceeds 0.85 during

449  most months. Due to the low-altitude and stable PBL in the colder months (from September to February), PM mass

450  concentrations in January, November, and December are high. Conversely, the lower PM concentrations occur during the

451  warmer months (from March to August), partly due to a higher PBL attributed to a stronger diurnal cycle, but also due to

452  higher precipitation in July and August. The AOD is generally high, implying severe aerosol loading in the YRD. As for the

453 mixed type of aerosol in the YRD, the volume size distributions show a bimodal logarithmic normal structure, except in June

454 and September, when it appears tri-modal due to hygroscopic growth. The highest SSA is also seen during these months.

455      During northern aerosol transportation, particles from polluted areas in North China are seen at a height of about 1–1.5

456 km, within the PBL, and are dominated by the fine mode, with $AOD_{440nm}$ above 0.65 and $SSA_{440nm}$ varying from 0.95 to 0.97.

457 A rising SSA indicates an increase in transported scattering particles, which decrease the radiation to the surface and cool the

458 surface. The weakening turbulence and the declining PBL lowers the aerosol layer and pollutants accumulate at lower

459 altitudes, thereby concentrating the scattering particles and forming a positive feedback mechanism.

460      Although dust transport to the YRD is seasonal and infrequent, it does make a difference to the YRD's aerosol loading.

461 Dust air masses around 2 km are transported from the northwestern desert regions including the Gurbantunggut Desert, the

462 Gobi Desert, and the Badain Duran Desert, and diffuses vertically with the lifting PBL. A significant increase in the coarse

463 mode at high altitudes brings about high concentrations of $PM_{10}$ and higher $AAOD_{440nm}$, illustrating the stronger absorptive

464 feature of transported dust compared to the northern pollutants transported over the YRD region. And the transported

465 absorptive dust particles heat the atmosphere, lifting PBL over YRD region to accelerate the diffusion in the PBL.

466      Biomass-burning pollutants also bring about a seasonal contribution to the aerosol loadings over the YRD region. In the

467 case of biomass-burning transportation, backward trajectories are consistent with the fire spots located in Guangdong, Fujian,

468 Jiangxi, and Zhejiang provinces south of the YRD, bringing absorptive fine particles to heights of about 1.5 km over that

469 region. The SSAs on most days are lower than 0.8 (except one day when the maximum $SSA_{440nm}$ is 0.898), indicating that

470 the biomass-burning pollutants transported from the southwest to the YRD can strengthen the absorptive ability in the

471 ambient atmosphere over the YRD.

472      The accumulation of locally emitted pollutants is facilitated by the low wind speed at the surface (10 m). During the

473 locally emitted aerosol case, the local aerosol layer appears below 1 km, and the low surface wind provides no external

474 transport. The mixture of locally emitted aerosols and dust particles transported downwards shows weaker absorption than

475 the biomass-burning products, and weaker scattering than the transported dust aerosols, with the $SSA_{440nm}$ varying from 0.86

476 to 0.91.

477      The haze pollution events that occur in the YRD region are not only affected by local emissions, but can also be

contributed to by regional transport, including pollutants from North China, dust aerosols from the northwestern deserts, and strong absorptive particles from southern biomass-burning areas. Therefore, air quality control should focus not only on local emissions reduction, but also on regional emissions.

**Acknowledgments**

This work was supported by grant from National Key R & D Program Pilot Projects of China (2016YFA0601901), National Natural Science Foundation of China (41590874&41375153), Natural Science Foundation of Zhejiang Province (LY16010006), the CAMS  Basis Research Project (2016Z001 & 2014R17), the Climate Change Special Fund of CMA (CCSF201504), CAMS Basic Research Project (2014R17), the Special Project of Doctoral Research supported by Liaoning Provincial Meteorological Bureau (D201501), Hangzhou Science and Technology Innovative project (20150533B17).

**References**

Ackerman, T. P., and Toon, O. B.: Absorption of visible radiation in atmosphere containing mixtures of absorbing and nonabsorbing particles, Appl Opt, 21, 3661-3667, 1981.

Adachi, K., Freney, E. J., and Buseck, P. R.: Shapes of internally mixed hygroscopic aerosol particles after deliquescence, and their effect on light scattering, Geophysical Research Letters, 38, 142-154, 2015.

Bond, T. C., Streets, D. G., Yarber, K. F., Nelson, S. M., Woo, J. H., and Klimont, Z.: A technology‐based global inventory of black and organic carbon emissions from combustion, Journal of Geophysical Research Atmospheres, 109, 1149-1165, 2004.

Bond, T. C., Doherty, S. J., Fahey, D. W., Forster, P. M., Berntsen, T., Deangelo, B. J., Flanner, M. G., Ghan, S., Kärcher, B., and Koch, D.: Bounding the role of black carbon in the climate system: A scientific assessment, Journal of Geophysical Research: Atmospheres, 118, 5380-5552, 2013.

Cao, J., Shen, Z., Chow, J. C., Qi, G., and Watson, J. G.: Seasonal variations and sources of mass and chemical composition

499   for PM 10 aerosol in Hangzhou, China, Particuology, 7, 161-168, 2009.

500  Cao, J. J., Wu, F., Chow, J. C., and Lee, S. C.: Characterization and source apportionment of atmospheric organic and

501   elemental carbon during fall and winter of 2003 in Xi'an, China, Atmospheric Chemistry & Physics, 5, 3127-3137,

502   2005.

503  Chan, C. K., and Yao, X.: Air pollution in mega cities in China, Atmospheric Environment, 42, 1-42, 2008.

504  Chan, K. L.: Biomass burning sources and their contributions to the local air quality in Hong Kong, Science of the Total

505   Environment, 596-597, 212, 2017.

506  Chauvigné, A., Sellegri, K., Hervo, M., Montoux, N., Freville, P., and Goloub, P.: Comparison of the aerosol optical

507   properties and size distribution retrieved by sun photometer with in situ measurements at midlatitude, 9, 4569-4585,

508   2016.

509  Che, H., Xia, X., Zhu, J., Li, Z., Dubovik, O., Holben, B., Goloub, P., Chen, H., Estelles, V., and Cuevasagulló, E.: Column

510   aerosol optical properties and aerosol radiative forcing during a serious haze-fog month over North China Plain in 2013

511   based on ground-based sunphotometer measurements, Atmospheric Chemistry & Physics, 14, 2125-2138, 2014.

512  Che, H., Zhang, X. Y., Xia, X., Goloub, P., Holben, B., Zhao, H., Wang, Y., Zhang, X. C., Wang, H., and Blarel, L.:

513   Ground-based aerosol climatology of China: aerosol optical depths from the China Aerosol Remote Sensing Network

514   (CARSNET) 2002-2013, Atmospheric Chemistry & Physics, 15, 7619-7652, 2015a.

515  Che, H., Zhao, H., Wu, Y., Xia, X., Zhu, J., Wang, H., Wang, Y., Sun, J., Yu, J., and Zhang, X.: Analyses of aerosol optical

516   properties and direct radiative forcing over urban and industrial regions in Northeast China, Meteorology and

517   Atmospheric Physics, 127, 345-354, 2015b.

518  Che, H. Z., Wang, Y. Q., Sun, J. Y., Zhang, X. C., Zhang, X. Y., and Guo, J. P.: Variation of Aerosol Optical Properties over

519   the Taklimakan Desert in China, Aerosol & Air Quality Research, 13, 777-785, 2013.

520  Chen, J., Jiang, H., Wang, B., Xiao, Z., Jiang, Z., Zhou, G., and Yu, S.: Aerosol optical properties from sun photometric

521   measurements in Hangzhou district, China, International Journal of Remote Sensing, 33, 2451-2461, 2012.

522  Chin, M., Diehl, T., Ginoux, P., and Yu, H.: Intercontinental Transport of Aerosols: Implication for Regional Air Quality,

523   AGU Spring Meeting, 2006.

524    Deardorff, J. W.: Parameterization of the Planetary Boundary layer for Use in General Circulation Models1, Monthly

525          Weather Review, 100, 93, 1972.

526    Ding, A., Fu, C., Yang, X., Sun, J., Petäjä, T., Kerminen, V.-M., Wang, T., Xie, Y., Herrmann, E., and Zheng, L.: Intense

527          atmospheric pollution modifies weather: a case of mixed biomass burning with fossil fuel combustion pollution in

528          eastern China, Atmospheric chemistry and physics, 13, 10545-10554, 2013.

529    Duan, J., and Mao, J.: Study on the Distribution and Variation Trends of Atmospheric Aerosol Optical Depth over the

530          Yangtze River Delta in China, Springer Netherlands, 361-370 pp., 2007.

531    Dubovik, O., Smirnov, A., Holben, B. N., King, M. D., Kaufman, Y. J., Eck, T. F., and Slutsker, I.: Accuracy assessments of

532          aerosol optical properties retrieved from Aerosol Robotic Network (AERONET) Sun and sky radiance measurements,

533          Journal of Geophysical Research Atmospheres, 105, 9791-9806, 2000.

534    Dubovik, O., Holben, B., Eck, T. F., Smirnov, A., Kaufman, Y. J., King, M. D., Tanré, D., and Slutsker, I.: Variability of

535          absorption and optical properties of key aerosol types observed in worldwide locations, Journal of the atmospheric

536          sciences, 59, 590-608, 2002.

537    Eck, T. F., Holben, B. N., Sinyuk, A., Pinker, R. T., Goloub, P., Chen, H., Chatenet, B., Li, Z., Singh, R. P., and Tripathi, S.

538          N.: Climatological aspects of the optical properties of fine/coarse mode aerosol mixtures, Journal of Geophysical

539          Research Atmospheres, 115, 19205, 2010.

540    Eck, T. F., Holben, B. N., Reid, J., Giles, D., Rivas, M., Singh, R. P., Tripathi, S., Bruegge, C., Platnick, S., and Arnold, G.:

541          Fog‐ and cloud‐induced aerosol modification observed by the Aerosol Robotic Network (AERONET), Journal of

542          Geophysical Research: Atmospheres, 117, 2012.

543    Fernald, F. G.: Analysis of atmospheric lidar observations: some comments, Applied Optics, 23, 652, 1984.

544    Fu, X., Wang, S. X., Cheng, Z., Xing, J., Zhao, B., Wang, J. D., and Hao, J. M.: Source, transport and impacts of a heavy

545          dust event in the Yangtze River Delta, China, in 2011, Atmospheric Chemistry & Physics, 14, 1239-1254, 2014.

546    Gao, Y., Zhang, M., Liu, Z., Wang, L., Wang, P., Xia, X., Tao, M., and Zhu, L.: Modeling the feedback between aerosol and

547          meteorological variables in the atmospheric boundary layer during a severe fog-haze event over the North China Plain,

548          Atmospheric Chemistry & Physics, 15, 1093-1130, 2015.

549    Gong, S., Zhang, X., Zhao, T., McKendry, I., Jaffe, D., and Lu, N.: Characterization of soil dust aerosol in China and its

550          transport and distribution during 2001 ACE‑Asia: 2. Model simulation and validation, Journal of Geophysical

551          Research: Atmospheres, 108, 2003.

552    Hansen, J., Sato, M., and Ruedy, R.: Radiative forcing and climate response, Journal of Geophysical Research, 102,

553          6831-6864, 1997.

554    He, Q., Li, C., Geng, F., Yang, H., Li, P., Li, T., Liu, D., and Pei, Z.: Aerosol optical properties retrieved from Sun

555          photometer measurements over Shanghai, China, Journal of Geophysical Research Atmospheres, 117, 81-81, 2012.

556    Holben, B. N., Eck, T. F., Slutsker, I., Tanr, D., eacute, Buis, J. P., Setzer, A., Vermote, E., Reagan, J. A., Kaufman, Y. J., and

557          Nakajima, T.: AERONET—A Federated Instrument Network and Data Archive for Aerosol Characterization,

558          Remote Sensing of Environment, 66, 1–16, 1998.

559    Holben, B. N., Tanré, D., Smirnov, A., Eck, T. F., Slutsker, I., Abuhassan, N., Newcomb, W. W., Schafer, J. S., Chatenet, B.,

560          and Lavenu, F.: An emerging ground-based aerosol climatology: Aerosol optical depth from AERONET, Journal of

561          Geophysical Research Atmospheres, 106, 12067–12097, 2001.

562    Hsu, Y. K., Holsen, T. M., and Hopke, P. K.: Comparison of hybrid receptor models to locate PCB sources in Chicago,

563          Atmospheric Environment, 37, 545-562, 2003.

564    Huang, X. X., Wang, T. J., Jiang, F., Liao, J. B., Cai, Y. F., Yin, C. Q., Zhu, J. L., and Han, Y.: Studies on a Severe Dust

565          Storm in East Asia and Its Impact on the Air Quality of Nanjing, China, Aerosol & Air Quality Research, 13, 179-193,

566          2013.

567    Ipcc, I.: IPCC Fourth Assessment Report: climate change 2007, 1340-1356, 2007.

568    Jacob, D. J., and Winner, D. A.: Effect Of Climate Change On Air Quality, Atmospheric Environment, 43, 51-63, 2009.

569    Jacobson, M. Z.: A physically‑based treatment of elemental carbon optics: Implications for global direct forcing of aerosols,

570          Geophysical Research Letters, 27, 217–220, 2000.

571    Jacobson, M. Z.: Strong radiative heating due to the mixing state of black carbon in atmospheric aerosols, Nature, 409,

572          695-697, 2001.

573    Jinyuan, Wupeng, WANG, Yuesi, Qingxian, Zhanqing, WANG, and Mingxing: Aerosol Optical Properties Affected by a

574    Strong Dust Storm over Central and Northern China, Advances in Atmospheric Sciences, 27, 562-574, 2010.

575    Kim, S. W., Yoon, S. C., Kim, J., Kang, J. Y., and Sugimoto, N.: Asian dust event observed in Seoul, Korea, during 29-31

576        May 2008: analysis of transport and vertical distribution of dust particles from lidar and surface measurements, Science

577        of the Total Environment, 408, 1707-1718, 2010.

578    Ku, J. Y., Hogrefe, C., Sistla, G., Chaw, S., Charles, L., and Gross, B.: Use of lidar backscatter to determine the PBL heights

579        in New York City, NY.

580    Leng, C., Duan, J., Xu, C., Zhang, H., Zhang, Q., Wang, Y., Li, X., Kong, L., Tao, J., and Cheng, T.: Insights into a historic

581        severe haze weather in Shanghai: synoptic situation, boundary layer and pollutants, Atmospheric Chemistry & Physics,

582        16, 9221-9234, 2015.

583    Levy, R. C., Remer, L. A., and Dubovik, O.: Global aerosol optical models and lookup tables for the new MODIS aerosol

584        retrieval over land, 2007a.

585    Levy, R. C., Remer, L. A., Mattoo, S., Vermote, E. F., and Kaufman, Y. J.: Second‐generation operational algorithm:

586        Retrieval of aerosol properties over land from inversion of Moderate Resolution Imaging Spectroradiometer spectral

587        reflectance, Journal of Geophysical Research Atmospheres, 112, 319-321, 2007b.

588    Lewis, J. R., Welton, E. J., Molod, A. M., and Joseph, E.: Improved boundary layer depth retrievals from MPLNET, Journal

589        of Geophysical Research-atmospheres, 118, 9870-9879, 2013.

590    Li, L., Huang, C., Huang, H. Y., Wang, Y. J., Yan, R. S., Zhang, G. F., Zhou, M., Lou, S. R., Tao, S. K., and Wang, H. L.: An

591        integrated process rate analysis of a regional fine particulate matter episode over Yangtze River Delta in 2010,

592        Atmospheric Environment, 91, 60-70, 2014.

593    Li, L., An, J. Y., Zhou, M., Yan, R. S., Huang, C., Lu, Q., Lin, L., Wang, Y. J., Tao, S. K., and Qiao, L. P.: Source

594        apportionment of fine particles and its chemical components over the Yangtze River Delta, China during a heavy haze

595        pollution episode, Atmospheric Environment, 123, 415-429, 2015.

596    Li, R.: Multi-Satellite Observation of an Intense Dust Event over Southwestern China, Aerosol & Air Quality Research, 15,

597        263-270, 2015.

598    Li, Z., Xia, X., Cribb, M., Mi, W., Holben, B., Wang, P., Chen, H., Tsay, S. C., Eck, T. F., and Zhao, F.: Aerosol optical

599     properties and their radiative effects in northern China, Journal of Geophysical Research Atmospheres, 112, 321-341,

600        2007.

601     Li, Z., Lau, W. K. M., Ramanathan, V., Wu, G., Ding, Y., Manoj, M. G., Liu, J., Qian, Y., Li, J., and Zhou, T.: Aerosol and

602        monsoon climate interactions over Asia, Reviews of Geophysics, 54, 2016.

603     Liu, G., Li, J., Wu, D., and Xu, H.: Chemical composition and source apportionment of the ambient PM 2.5 in Hangzhou,

604        China, Particuology, 18, 135-143, 2015.

605     Liu, J., Zheng, Y., Li, Z., Flynn, C., Welton, E. J., and Cribb, M.: Transport, vertical structure and radiative properties of dust

606        events in southeast China determined from ground and space sensors, Atmospheric Environment, 45, 6469-6480, 2011.

607     Liu, Q., He, Q., Fang, S., Ying, G., Ma, C., Chen, Y., Kang, Y., Hu, P., Hua, Z., and Yao, Y.: Vertical distribution of ambient

608        aerosol extinctive properties during haze and haze-free periods based on the Micro-Pulse Lidar observation in Shanghai,

609        Science of the Total Environment, 574, 1502-1511, 2016.

610     Liu, S. Y., and Liang, X. Z.: Observed diurnal cycle climatology of planetary boundary layer height, Journal of Climate, 23,

611        5790-5809, 2010.

612     Martins, J. V., Artaxo, P., Liousse, C., Reid, J. S., Hobbs, P. V., and Kaufman, Y. J.: Effects of black carbon content, particle

613        size, and mixing on light absorption by aerosols from biomass burning in Brazil, Journal of Geophysical Research

614        Atmospheres, 103, 32041-32050, 1998.

615     Medeiros, B., Hall, A., and Stevens, B.: What Controls the Mean Depth of the PBL?, Journal of Climate, 18, 3157-3172,

616        2005.

617     Ming, L., Jin, L., Li, J., Fu, P., Yang, W., Liu, D., Zhang, G., Wang, Z., and Li, X.: PM2.5 in the Yangtze River Delta, China:

618        Chemical compositions, seasonal variations, and regional pollution events, Environmental Pollution, 223, 200, 2017.

619     Ngan, F., Stein, A., and Draxler, R.: Inline Coupling of WRF-HYSPLIT: Model Development and Evaluation Using Tracer

620        Experiments, Journal of Applied Meteorology & Climatology, 54, 150330095210006, 2015.

621     Omar, A. H., Winker, D. M., Vaughan, M. A., Hu, Y., Trepte, C. R., Ferrare, R. A., Lee, K.-P., Hostetler, C. A., Kittaka, C.,

622        and Rogers, R. R.: The CALIPSO automated aerosol classification and lidar ratio selection algorithm, Journal of

623        Atmospheric and Oceanic Technology, 26, 1994-2014, 2009.

624  Pan, L., Che, H., Geng, F., Xia, X., Wang, Y., Zhu, C., Chen, M., Gao, W., and Guo, J.: Aerosol optical properties based on

625      ground measurements over the Chinese Yangtze Delta Region, Atmospheric Environment, 44, 2587-2596, 2010.

626  Petäjä, T., Järvi, L., Kerminen, V. M., Ding, A. J., Sun, J. N., Nie, W., Kujansuu, J., Virkkula, A., Yang, X., and Fu, C. B.:

627      Enhanced air pollution via aerosol-boundary layer feedback in China, Scientific Reports, 6, 18998, 2016.

628  Pilat, M. J., and Charlson, R. J.: Theoretical and optical studies of humidity effects on the size distribution of a hygroscopic

629      aerosol, J. Rech. Atmos, 2, 166-170, 1966.

630  Polissar, A. V., Hopke, P. K., Paatero, P., Kaufmann, Y. J., Hall, D. K., Bodhaine, B. A., Dutton, E. G., and Harris, J. M.: The

631      aerosol at Barrow, Alaska: long-term trends and source locations, Atmospheric Environment, 33, 2441-2458, 1999.

632  Qi, B.: Seasonal Variation of Aerosol Optical Properties in an Urban Site of the Yangtze Delta Region of China, Aerosol &

633      Air Quality Research, 16, 2016.

634  Sakai, T., Shibata, T., Iwasaka, Y., Nagai, T., Nakazato, M., Matsumura, T., Ichiki, A., Kim, Y. S., Tamura, K., and Troshkin,

635      D.: Case study of Raman lidar measurements of Asian dust events in 2000 and 2001 at Nagoya and Tsukuba, Japan,

636      Atmospheric Environment, 36, 5479-5489, 2002.

637  Sakai, T., Nagai, T., Nakazato, M., Mano, Y., and Matsumura, T.: Ice clouds and Asian dust studied with lidar measurements

638      of particle extinction-to-backscatter ratio, particle depolarization, and water-vapor mixing ratio over Tsukuba, Applied

639      Optics, 42, 7103-7116, 2003.

640  Seibert, P., Kromp-Kolb, H., Baltensperger, U., Jost, D. T., and Schwikowski, M.: Trajectory Analysis of High-Alpine Air

641      Pollution Data, Springer US, 253-269 pp., 1994.

642  Sirois, A., and Bottenheim, J. W.: Use of backward trajectories to interpret the 5‐year record of PAN and O3 ambient air

643      concentrations at Kejimkujik National Park, Nova Scotia, Journal of Geophysical Research Atmospheres, 100,

644      2867-2882, 1995.

645  Stocker, T. F., Qin, D., Plattner, G.-K., Tignor, M., Allen, S. K., Boschung, J., Nauels, A., Xia, Y., Bex, B., and Midgley, B.:

646      IPCC, 2013: climate change 2013: the physical science basis. Contribution of working group I to the fifth assessment

647      report of the intergovernmental panel on climate change, in, Cambridge University Press, 2013.

648  Sun, T., Che, H., Wu, J., Wang, H., Wang, Y., and Zhang, X.: The variation in visibility and its relationship with surface wind

649      speed in China from 1960 to 2009, Theoretical & Applied Climatology, 1-13, 2016.

650    Tao, M., Chen, L., Su, L., and Tao, J.: Satellite observation of regional haze pollution over the North China Plain, Journal of

651      Geophysical Research: Atmospheres, 117, 12203, 2012.

652    Tao, M., Chen, L., Li, R., Wang, L., Wang, J., Wang, Z., Tang, G., and Tao, J.: Spatial oscillation of the particle pollution in

653      eastern China during winter: Implications for regional air quality and climate, Atmospheric Environment, 144, 100-110,

654      2016.

655    Uno, I., Eguchi, K., Yumimoto, K., Takemura, T., Shimizu, A., Uematsu, M., Liu, Z., Wang, Z., Hara, Y., and Sugimoto, N.:

656      Asian dust transported one full circuit around the|[nbsp]|globe, 2, 2009.

657    Vaughan, M., Young, S., Winker, D., Powell, K., Omar, A., Liu, Z., Hu, Y., and Hostetler, C.: Fully automated analysis of

658      space-based lidar data: An overview of the CALIPSO retrieval algorithms and data products, Proc. of SPIE Vol, 2004,

659      17.

660    Wang, S. X., and Zhang, C. Y.: Spatial and temporal distribution of air pollutant emissions from open burning of crop

661      residues in China, Sciencepaper Online, 2008.

662    Wang, Y., Zhuang, G., Zhang, X., Huang, K., Xu, C., Tang, A., Chen, J., and An, Z.: The ion chemistry, seasonal cycle, and

663      sources of PM 2.5 and TSP aerosol in Shanghai, Atmospheric Environment, 40, 2935-2952, 2006a.

664    Wang, Y. Q., Zhang, X. Y., and Arimoto, R.: The contribution from distant dust sources to the atmospheric particulate matter

665      loadings at XiAn, China during spring, Science of the Total Environment, 368, 875, 2006b.

666    Winker, D. M., Vaughan, M. A., Omar, A., Hu, Y., Powell, K. A., Liu, Z., Hunt, W. H., and Young, S. A.: Overview of the

667      CALIPSO mission and CALIOP data processing algorithms, Journal of Atmospheric and Oceanic Technology, 26,

668      2310-2323, 2009.

669    Wu, J., Fu, C., Zhang, L., and Tang, J.: Trends of visibility on sunny days in China in the recent 50 years, Atmospheric

670      Environment, 55, 339-346, 2012.

671    Wu, Y., Han, Y., Voulgarakis, A., Wang, T., Li, M., Wang, Y., Xie, M., Zhuang, B., and Li, S.: An agricultural biomass

672      burning episode in eastern China: Transport, optical properties, and impacts on regional air quality, Journal of

673      Geophysical Research Atmospheres, 122, 2017.

674  Xia, X., Li, Z., Holben, B., Wang, P., Eck, T., Chen, H., Cribb, M., and Zhao, Y.: Aerosol optical properties and radiative

675    effects in the Yangtze Delta region of China, Journal of Geophysical Research Atmospheres, 112, 449-456, 2007.

676  Xia, X., Chen, H., Goloub, P., Zong, X., Zhang, W., and Wang, P.: Climatological aspects of aerosol optical properties in

677    North China Plain based on ground and satellite remote-sensing data, Journal of Quantitative Spectroscopy & Radiative

678    Transfer, 127, 12-23, 2013.

679  Xiao, Z.-m., Zhang, Y.-f., Hong, S.-m., Bi, X.-h., Jiao, L., Feng, Y.-c., and Wang, Y.-q.: Estimation of the main factors

680    influencing haze, based on a long-term monitoring campaign in Hangzhou, China, Aerosol and Air Quality Resarch, 11,

681    873-882, 2011.

682  Xin, Y.: Identification of Long-Range Transport Pathways and Potential Sources of PM10 in Tibetan Plateau Uplift Area:

683    Case Study of Xining, China in 2014, Aerosol & Air Quality Research, 16, 1044-1054, 2016.

684  Yong, H., Wu, Y., Wang, T., Xie, C., Zhao, K., Zhuang, B., and Li, S.: Characterizing a persistent Asian dust transport event:

685    optical properties and impact on air quality through the ground-based and satellite measurements over Nanjing, China,

686    Atmospheric Environment, 115, 304-316, 2015.

687  Zhang, J., Wang, L., Chen, J., Feng, S., Shen, J., and Jiao, L.: Hygroscopicity of ambient submicron particles in urban

688    Hangzhou, China, Frontiers of Environmental Science & Engineering, 5, 342-347, 2011.

689  Zhang, J., and Li, X.: Vertical distribution of sand-dust aerosols and the relationships with atmospheric environment, Journal

690    of Arid Land, 4, 357-368, 2012.

691  Zhang, R., Jing, J., Tao, J., and Hsu, S. C.: Chemical characterization and source apportionment of PM2.5 in Beijing:

692    seasonal perspective, Atmospheric Chemistry & Physics Discussions, 13, 7053-7074, 2013.

693  Zhang, X. Y., Arimoto, R., Zhu, G. H., Chen, T., and Zhang, G. Y.: Concentration, size‐distribution and deposition of

694    mineral aerosol over Chinese desert regions, Tellus Series B-chemical & Physical Meteorology, 50, 317-330, 1998.

695  Zhang, X. Y., Wang, Y. Q., Niu, T., Zhang, X. C., Gong, S. L., Zhang, Y. M., and Sun, J. Y.: Corrigendum to "Atmospheric

696    aerosol compositions in China: spatial/temporal variability, chemical signature, regional haze distribution and

697    comparisons with global aerosols " published in Atmos. Chem. Phys., 12, 779–799, 2012, Atmospheric Chemistry &

698    Physics, 11, 26571-26615, 2012.

699    Zhang, Z., Zhou, W., Wenig, M., and Yang, L.: Impact of long-range desert dust transport on coastal East Asia: analysis of

700        urban dust concentration and wet deposition with model simulation, Air Quality Atmosphere & Health, 1-13, 2016.

701    Zhu, J., Che, H., Xia, X., Chen, H., Goloub, P., and Zhang, W.: Column-integrated aerosol optical and physical properties at

702        a regional background atmosphere in North China Plain, Atmospheric Environment, 84, 54-64, 2014.

703    Zhuang, B. L., Wang, T. J., Liu, J., Ma, Y., Yin, C. Q., Li, S., Xie, M., Han, Y., Zhu, J. L., and Yang, X. Q.: Absorption

704        coefficient of urban aerosol in Nanjing, west Yangtze River Delta of China, Atmospheric Chemistry & Physics, 15,

705        16175-16213, 2015.

706

707
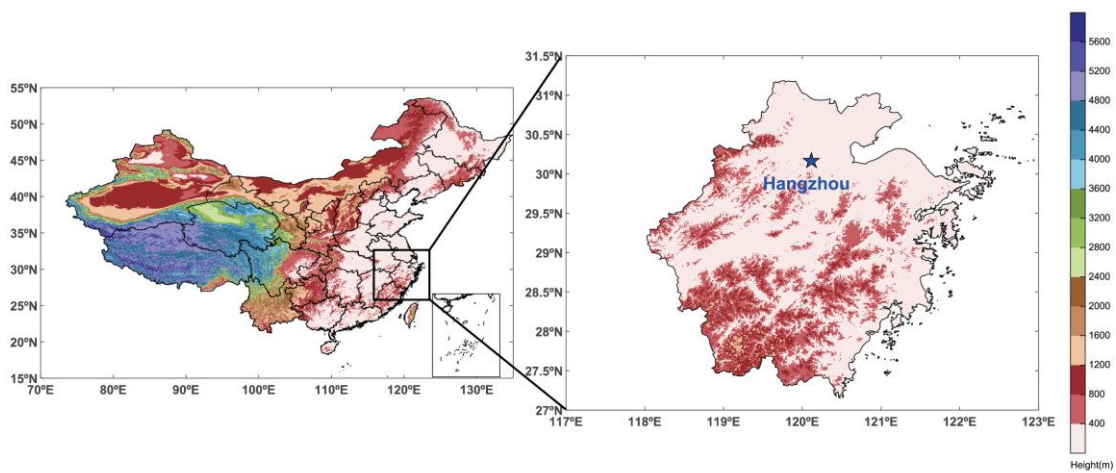
Figure 1. Terrain elevation and location of the Yangtze River Delta region in China.

712
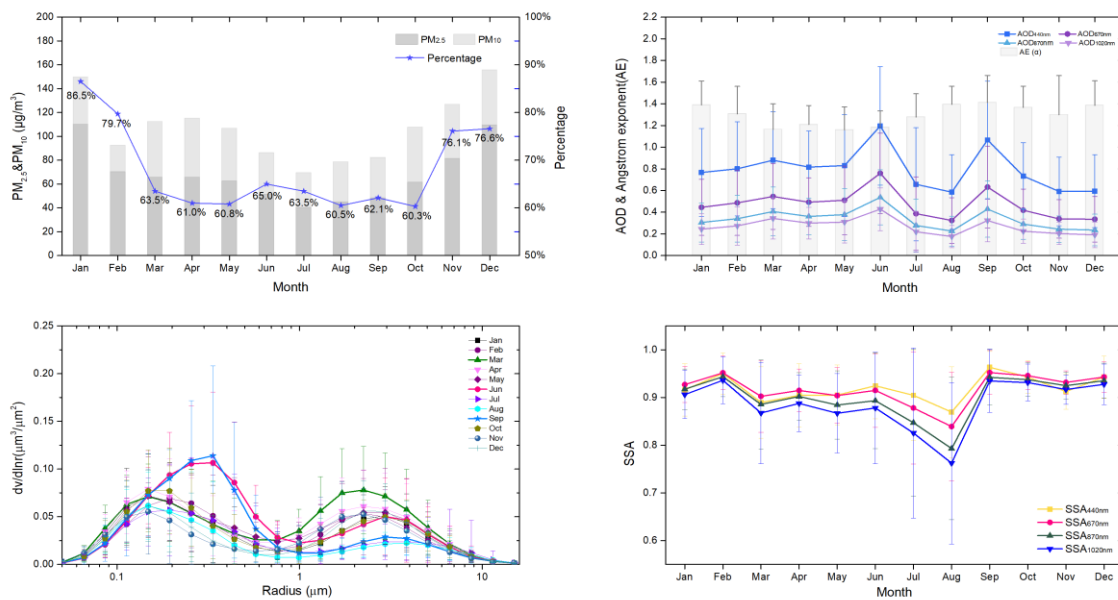
**Figure 2. Monthly variation in averaged (a) mass concentration of PM$_{2.5}$ and PM$_{10}$, (b) AOD (440, 670, 870, and 1020 nm) and AE**

**(between 440 and 870 nm), (c) volume size distribution, (d) SSA (440, 670, 870, and 1020 nm), during 2013–2015 in Hangzhou.**

715

716

717
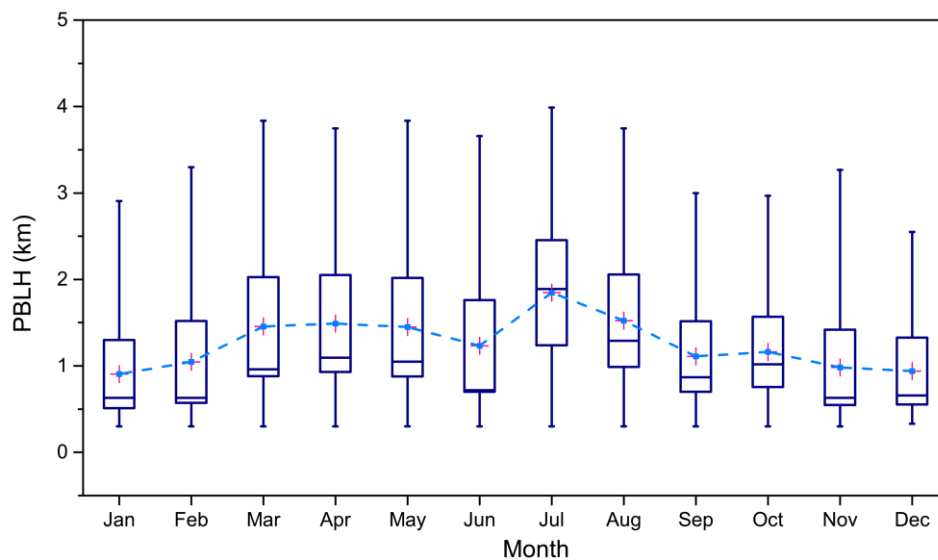
**Figure 3. Monthly variation of averaged PBLH retrieved from the MPL, and their 5th and 95th percentile box plots during 2013–**

**2015 in Hangzhou.**

720
721

722
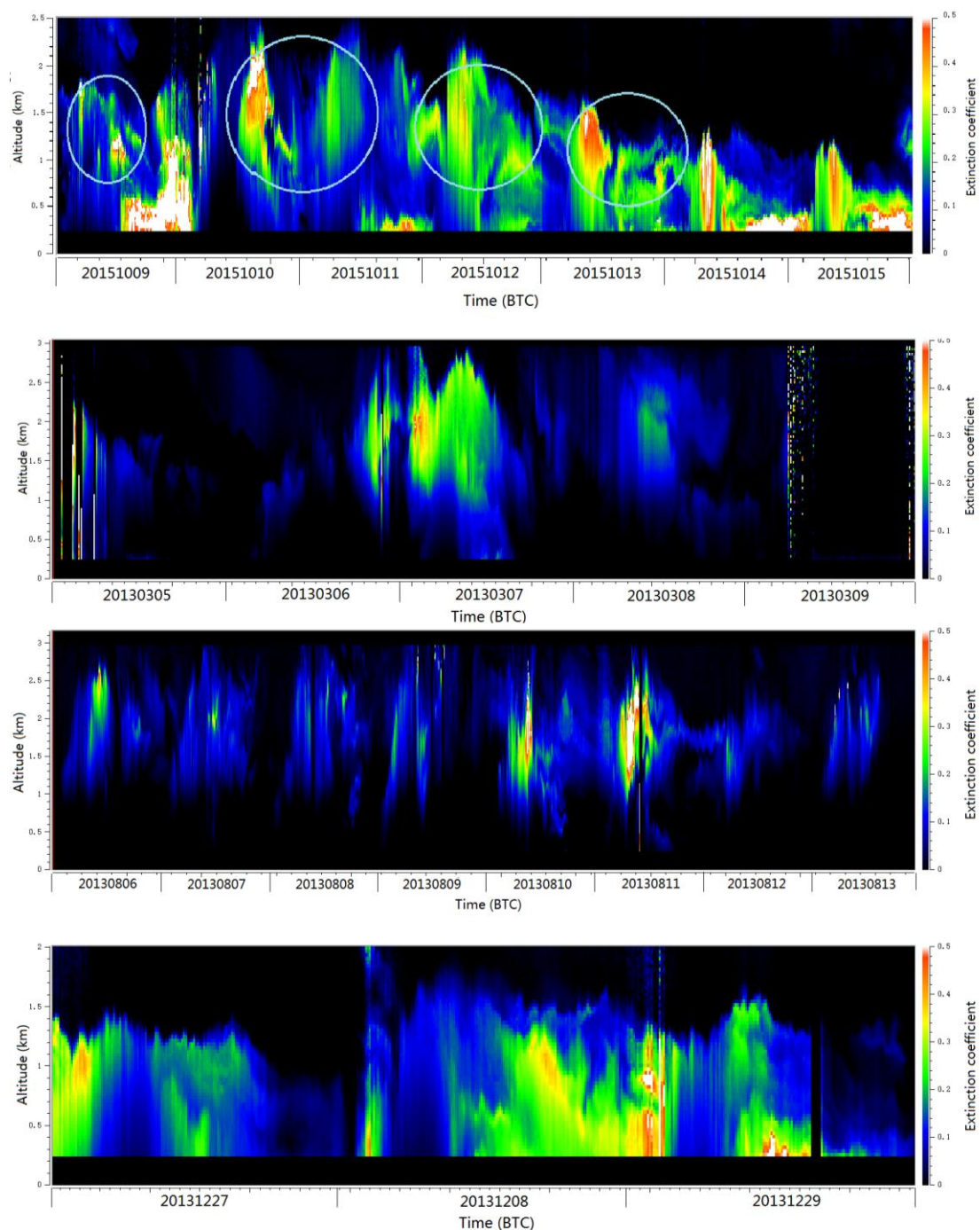
Figure 4. Time–height cross section of the ground-based lidar-derived extinction coefficient at 532 nm in Hangzhou during (a) 9–15
October 2015, (b) 5–9 March 2013, (c) 6–13 August 2013, and (d) 27–29 December 2013.
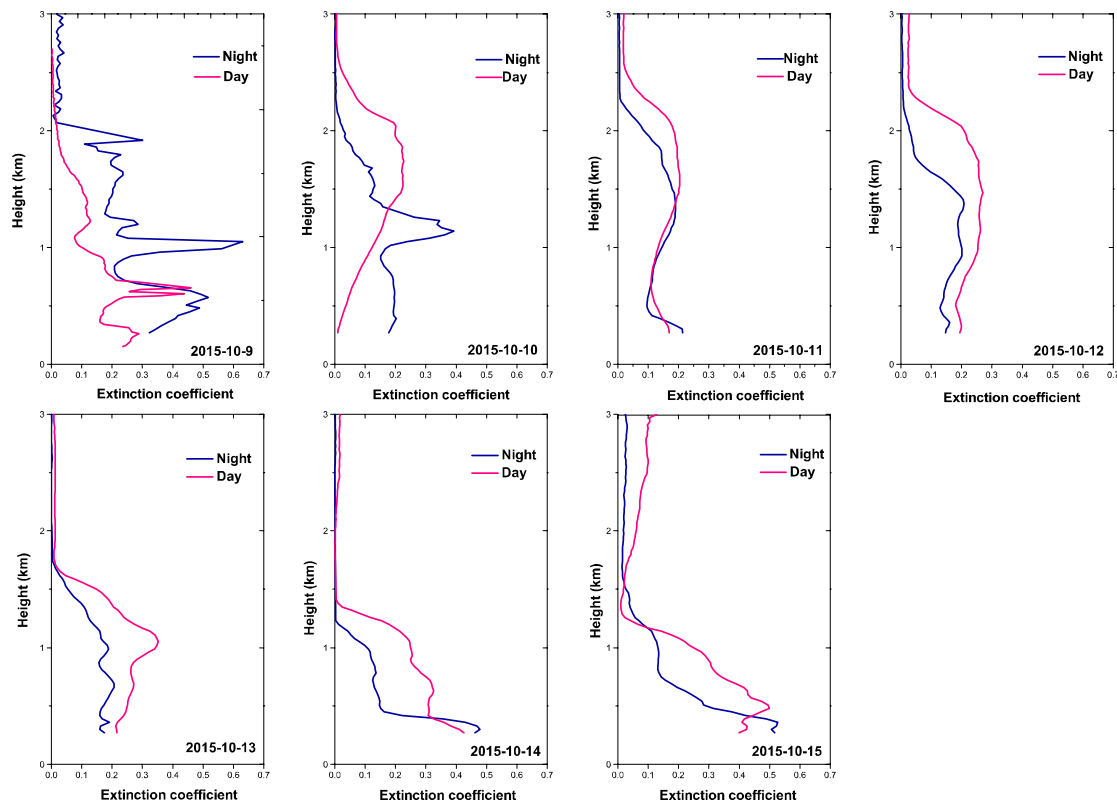
**Figure 5.** Profiles of the aerosol extinction coefficient from MPL-retrieved data, averaged for daytime and nighttime during 9–15 October 2015 in Hangzhou.
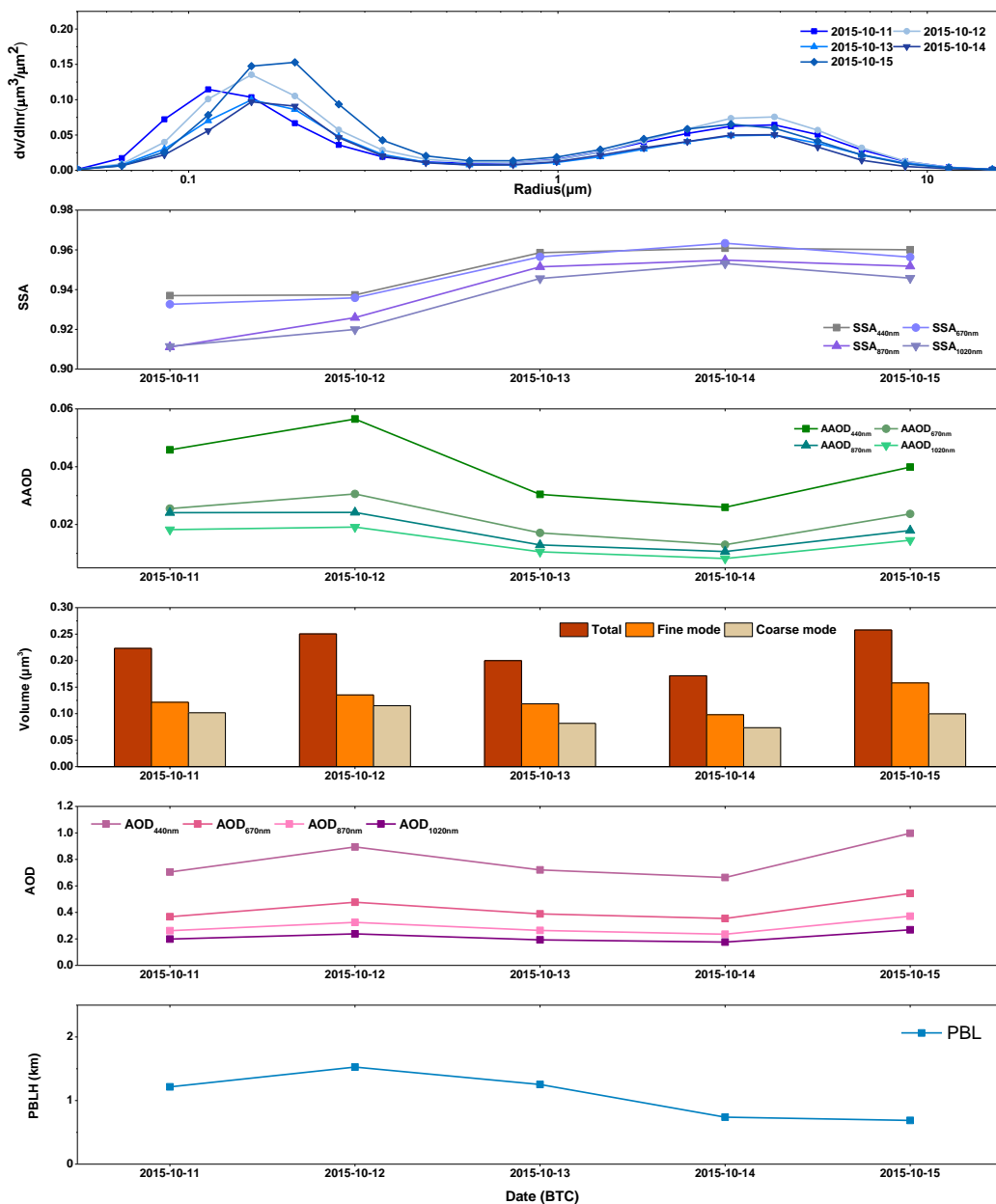
732

733    **Figure 6. Daily averaged variation in aerosol optical properties and PBLH in Hangzhou during 11–15 October 2015.**

734

735

736
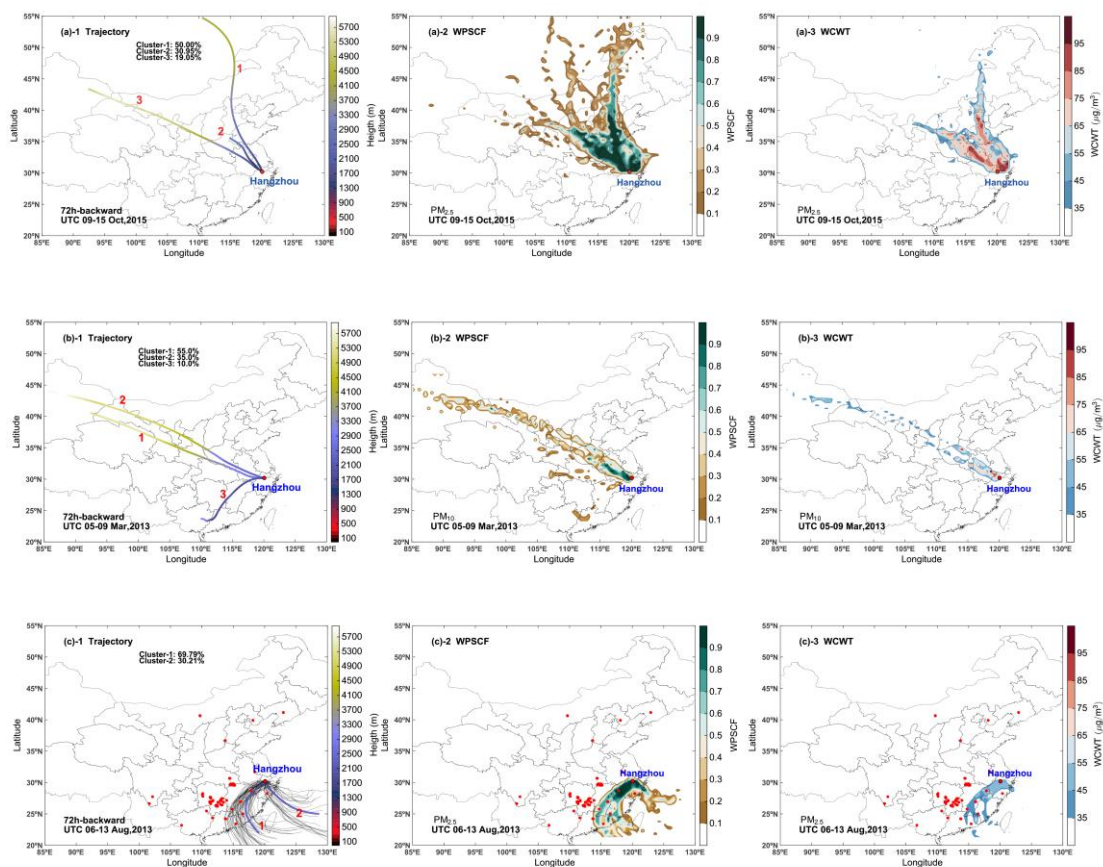
**Figure 7. Mean 72-h backward trajectories of each trajectory cluster and spatial distributions of WPSCF and WCWT values for**

**PM2.5 in Hangzhou during (a) 9–15 October 2015, (b) 5–9 March 2013, and (c) 6–13 August 2013.**

739

740
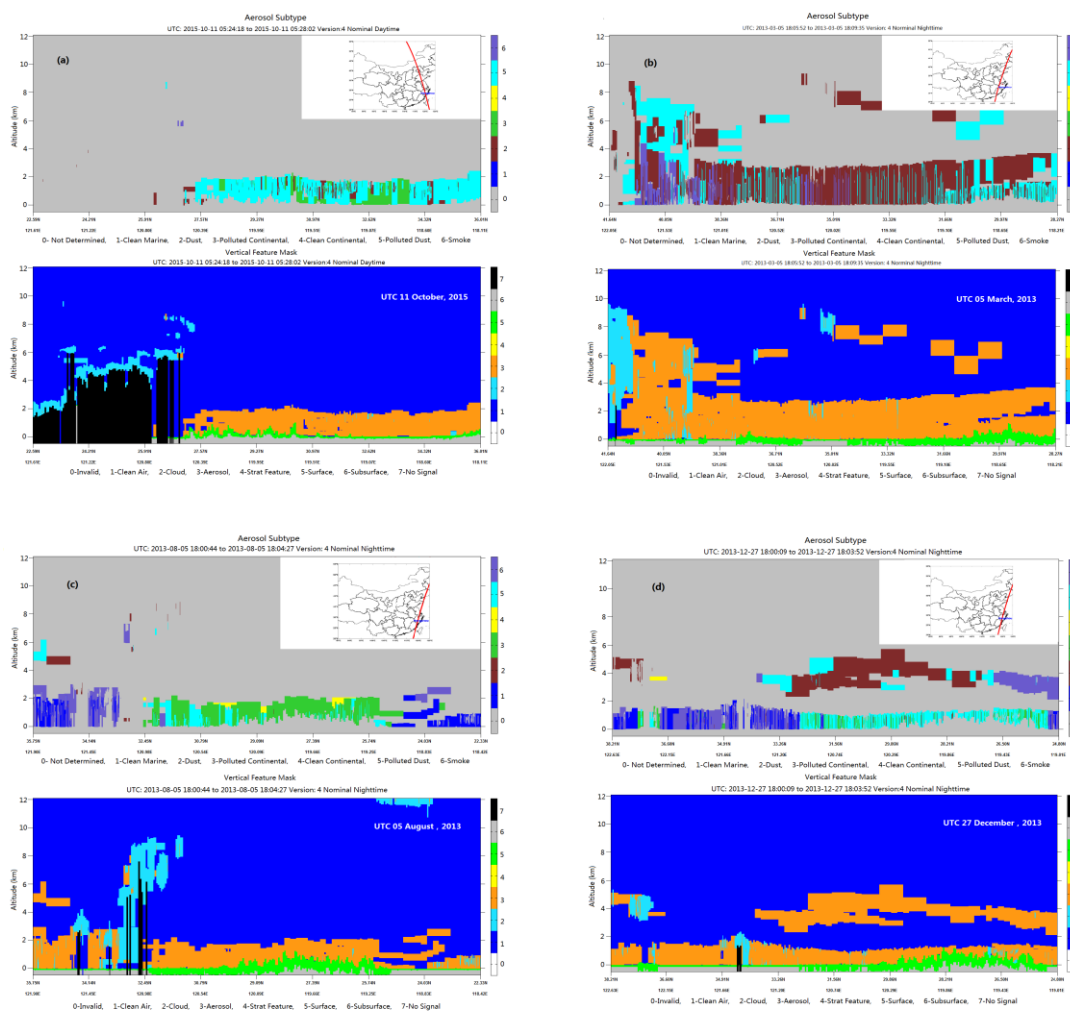
**Figure 8. CALIPSO L2 products of vertical feature mask, aerosol subtype, and its ground track on (a) 11 October 2015, (b) 5 March 2013, (c) 5 August 2013, and (d) 27 December 2013.**
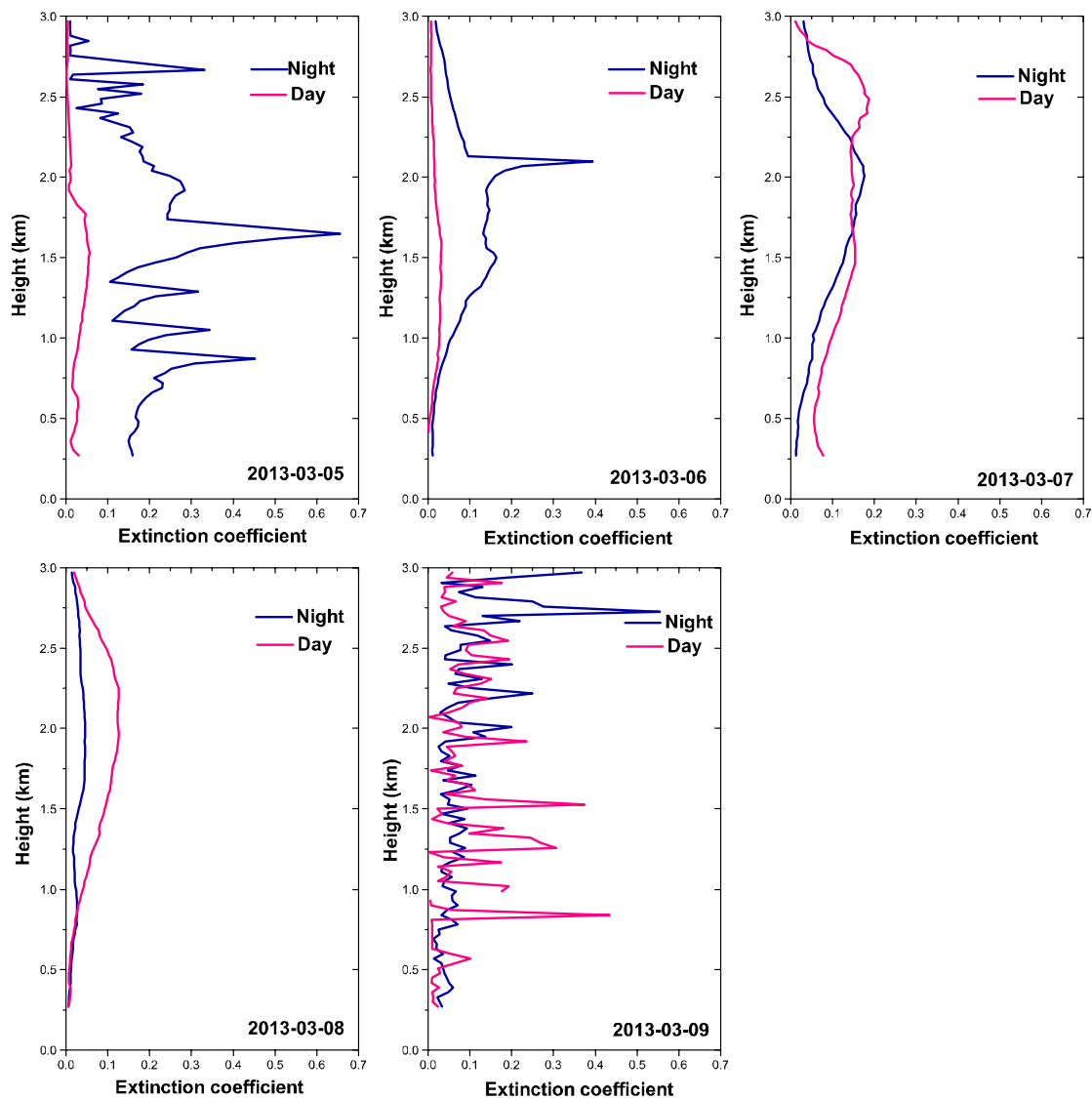
Figure 9. Profiles of aerosol extinction coefficient from MPL-retrieved data averaged for daytime and nighttime during 5–9 March

2013 in Hangzhou.

751
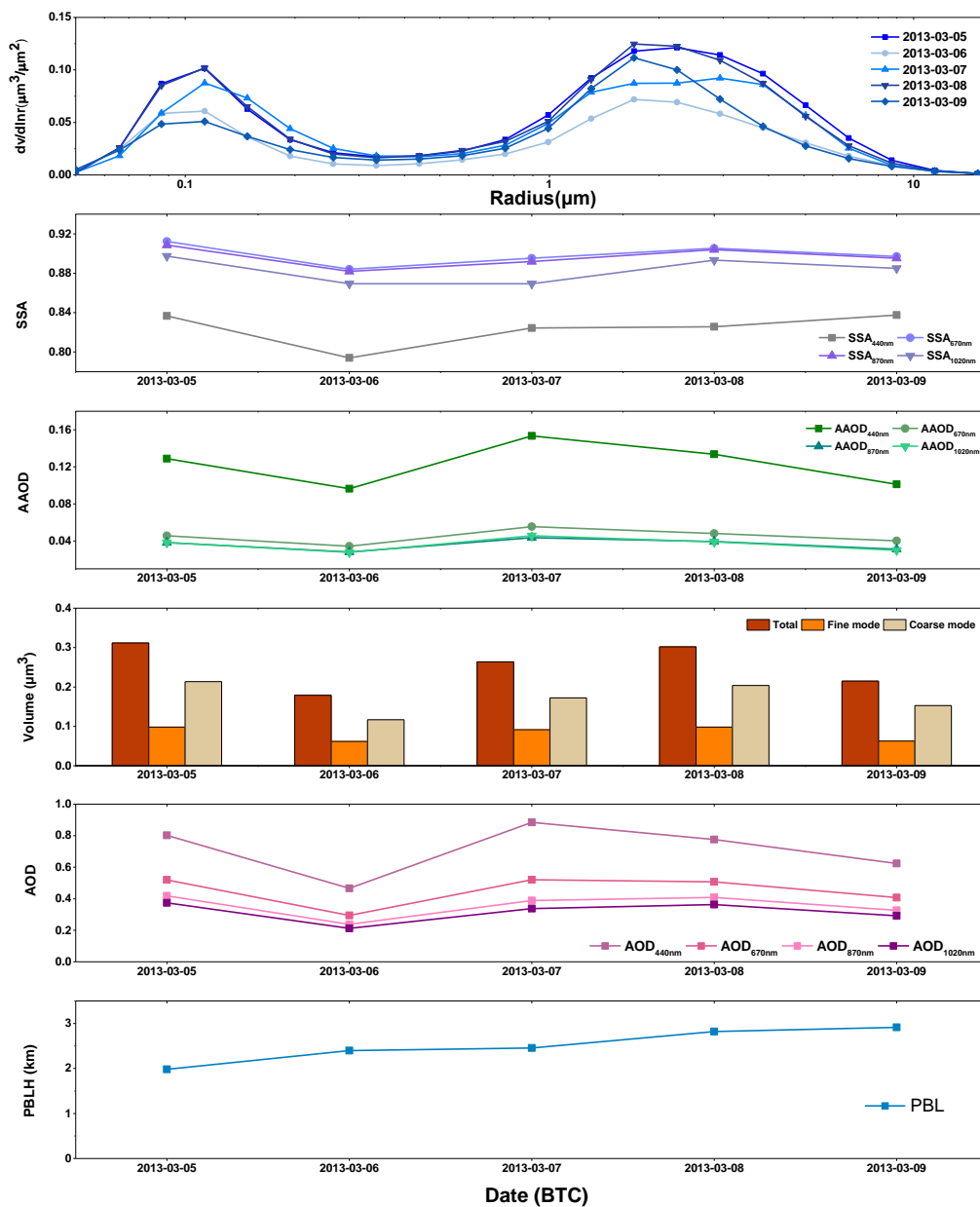
**Figure 10. Daily averaged variation in aerosol optical properties and the PBLH in Hangzhou during 5–9 March 2013.**

753

754
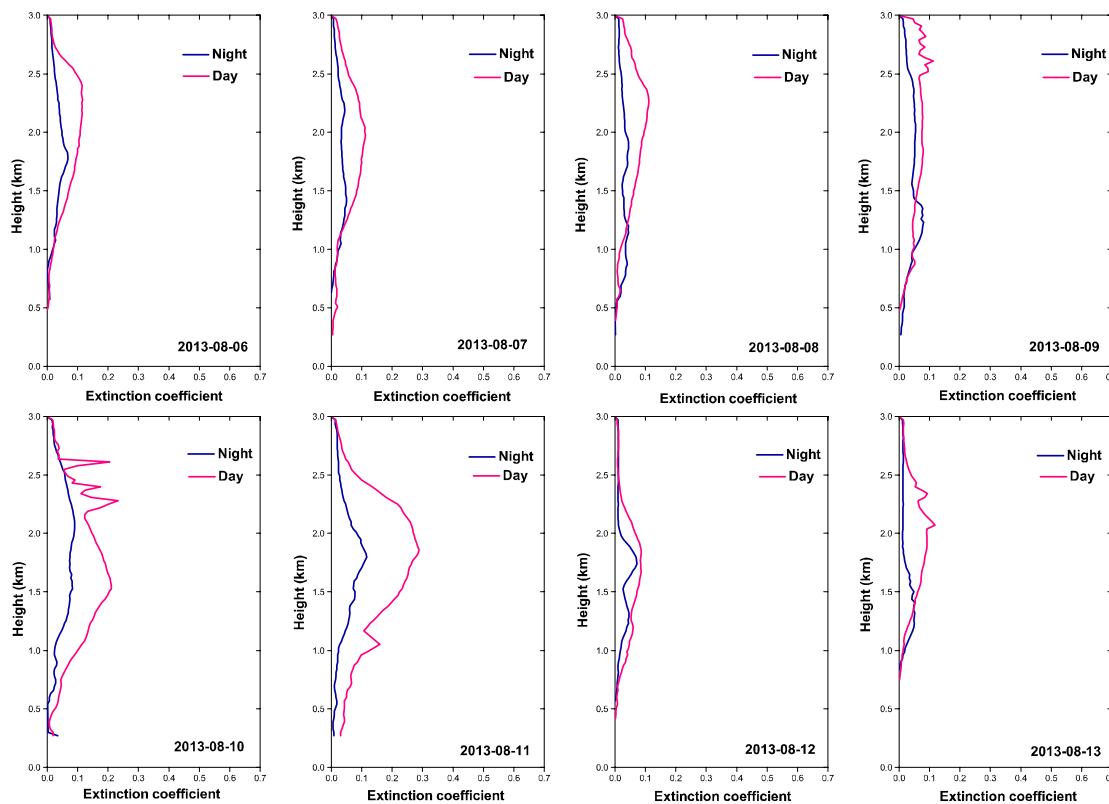
**Figure 11. Profiles of the aerosol extinction coefficient from MPL-retrieved data averaged for daytime and nighttime during 6–13**

**August 2013 in Hangzhou.**
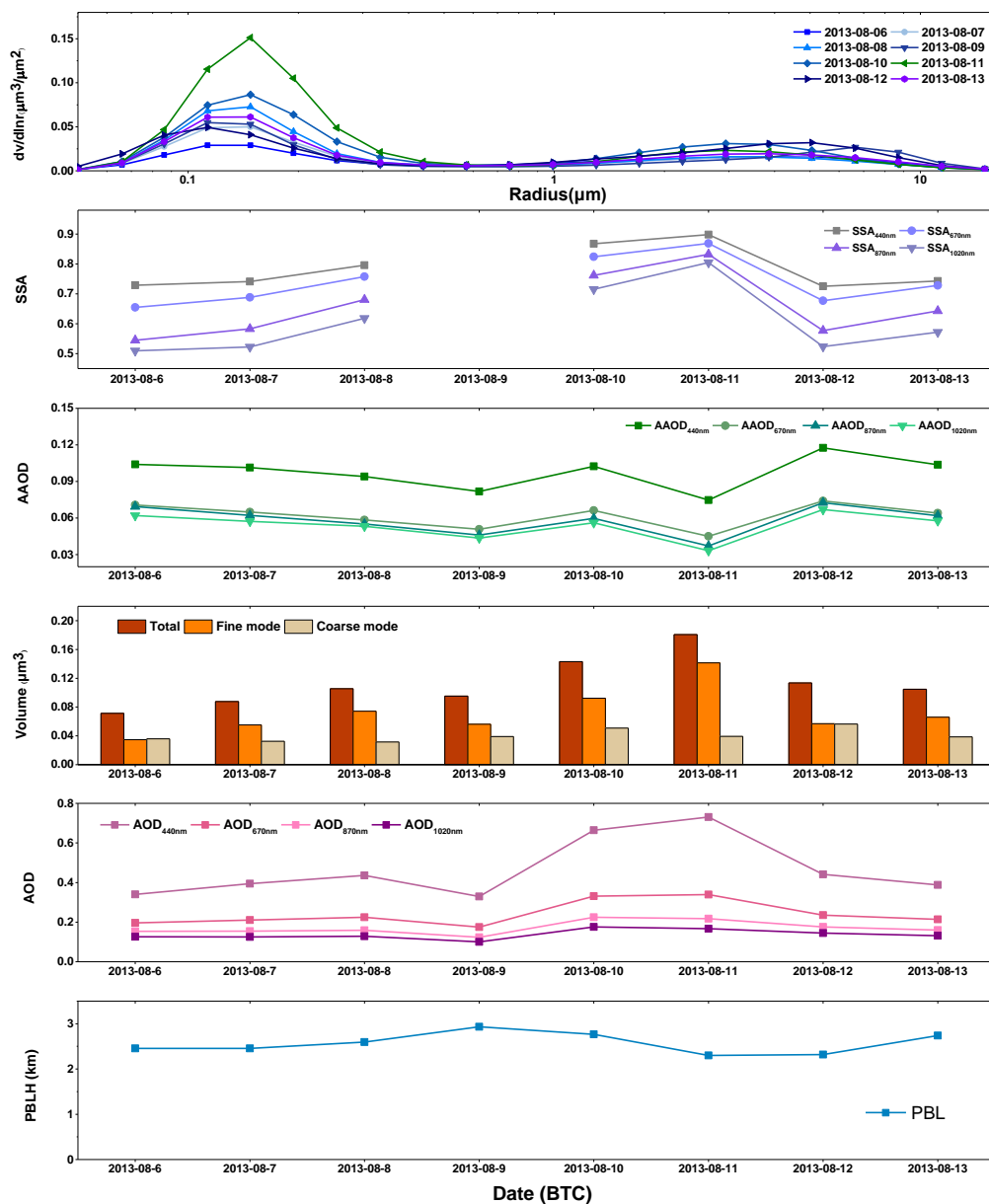
**Figure 12. Daily averaged variation of aerosol optical properties and PBLHs in Hangzhou during 6–13 August 2013.**
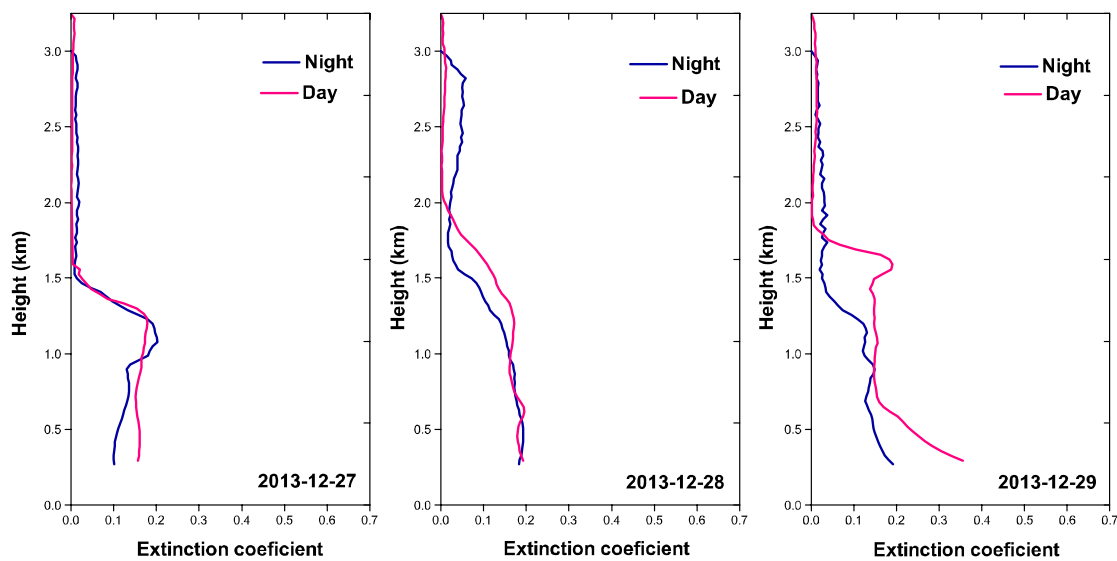
**Figure 13. Profiles of aerosol extinction coefficient from MPL-retrieved data averaged for daytime and nighttime during 27–29 December 2013 in Hangzhou.**
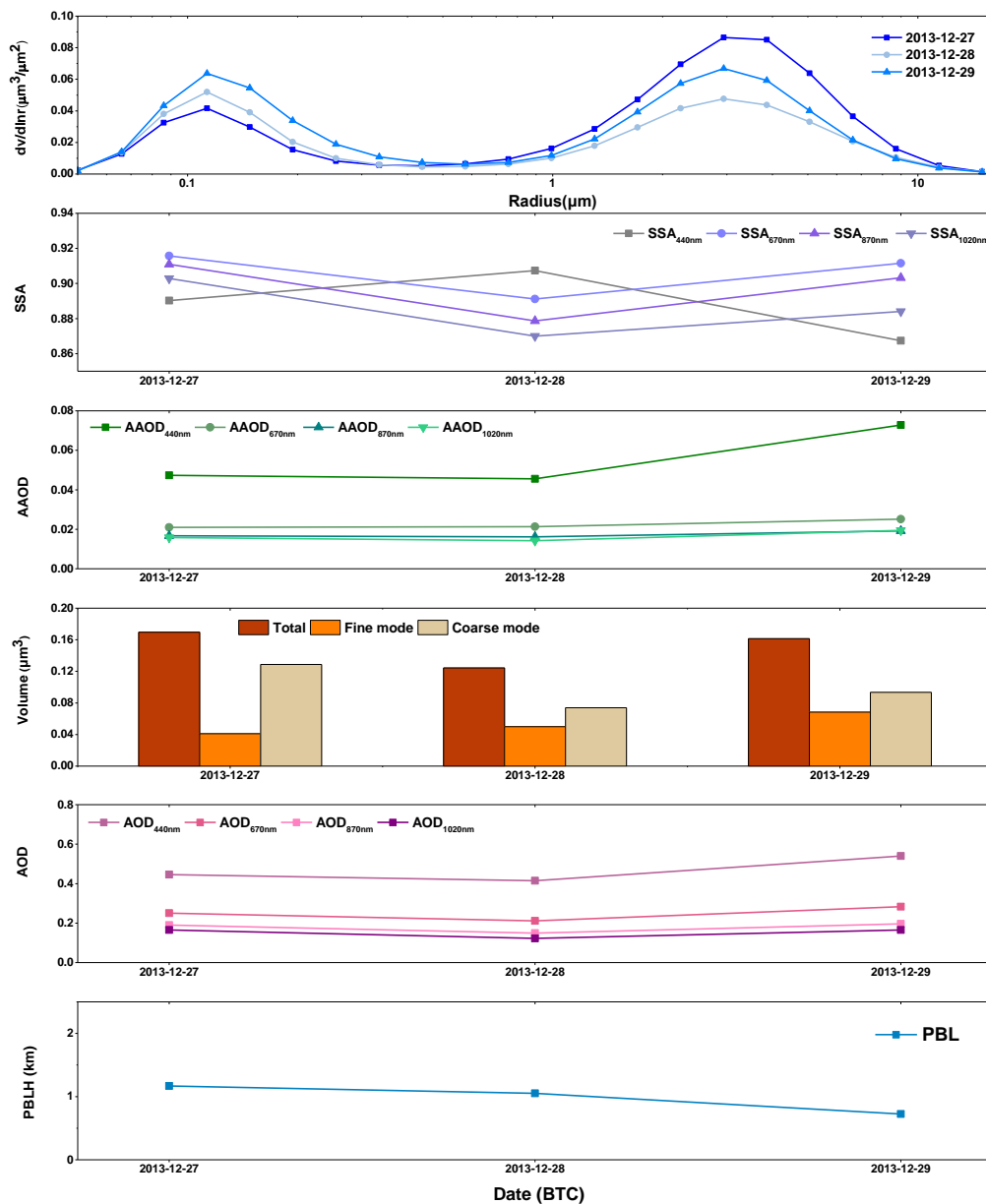
**Figure 14. Daily averaged variation in aerosol optical properties and the PBLH in Hangzhou during 27–29 December 2013.**

771

772

773

774

| Case | Cluster | Number | Mean (µg /m$^3$) |
|------|---------|--------|------------------|
| **1** | 1 | 41 | 81.05±28.18 |
|  | 2 | 22 | 74.45±30.17 |
|  | 3 | 9 | 76.11±35.51 |
| **2** | 1 | 12 | 71.08±60.00 |
|  | 2 | 7 | 84.57±18.26 |
| **3** | 1 | 61 | 54.52±16.63 |
|  | 2 | 26 | 39.04±10.14 |

775

776 **Table 1. Trajectory number and PM mean concentration of each cluster in Hangzhou during three cases, including case 1**

777 **(transportation from haze area of North China), case 2 (transportation from northwestern dust area), case 3(transportation from**

778 **southern biomass burning area).**

779

780